JGR Atmospheres

RESEARCH ARTICLE
10.1029/2019JD030932

This article is a companion to Fritts et al. (2019), https://doi.org/10.1029/2019jd030899.

Key Points:
- Multi-instrument characterization of a mesospheric mountain wave exhibit a unique, large-amplitude "saw-tooth" wave breaking signature
- Unexpected large-amplitude mesospheric mountain waves accompany weak winds over low orography due to favorable propagation conditions
- Very large mesospheric mountain wave momentum fluxes ~400-800 m^2/s^2 are sustained for multiple wave periods

Supporting Information:
- Supporting Information S1

Correspondence to:
M. J. Taylor,
mike.taylor@usu.edu

Citation:
Taylor, M. J., Pautet, P.-D., Fritts, D. C., Kaifler, B., Smith, S. M., Zhao, Y., et al. (2019). Large-amplitude mountain waves in the mesosphere observed on 21 June 2014 during DEEPWAVE: 1. Wave development, scales, momentum fluxes, and environmental sensitivity. *Journal of Geophysical Research: Atmospheres*, *124*, 10,364–10,384. https://doi.org/10.1029/2019JD030932

Received 2 MAY 2019
Accepted 9 AUG 2019
Accepted article online 6 SEP 2019
Published online 15 OCT 2019

Large-Amplitude Mountain Waves in the Mesosphere Observed on 21 June 2014 During DEEPWAVE: 1. Wave Development, Scales, Momentum Fluxes, and Environmental Sensitivity

Michael J. Taylor[1], Pierre-Dominique Pautet[1], David C. Fritts[2], Bernd Kaifler[3], Steven M. Smith[4], Yucheng Zhao[1], Neal R. Criddle[1], Pattilyn McLaughlin[1], William R. Pendleton Jr.[1], Michael P. McCarthy[5], Gonzalo Hernandez[5,6], Stephen D. Eckermann[7], James Doyle[8], Markus Rapp[3], Ben Liley[9], and James M. Russell III[10]

[1]Center for Atmospheric and Space Sciences, Utah State University, Logan, UT, [2]GATS Inc., Boulder, CO, USA, [3]German Aerospace Center (DLR), Munich, Germany, [4]Center for Space Physics, Boston University, Boston, MA, [5]Earth and Space Sciences, University of Washington, Seattle, WA, USA, [6]Deceased July 15, 2014, [7]Naval Research Laboratory, Washington, DC, USA, [8]James Doyle, Naval Research Laboratory, Monterey, CA, USA, [9]National Institute of Water and Atmospheric Research, Auckland, New Zealand, [10]Center for Atmospheric Science, Hampton University, Hampton, VA, USA

Abstract A remarkable, large-amplitude, mountain wave (MW) breaking event was observed on the night of 21 June 2014 by ground-based optical instruments operated on the New Zealand South Island during the Deep Propagating Gravity Wave Experiment (DEEPWAVE). Concurrent measurements of the MW structures, amplitudes, and background environment were made using an Advanced Mesospheric Temperature Mapper, a Rayleigh Lidar, an All-Sky Imager, and a Fabry-Perot Interferometer. The MW event was observed primarily in the OH airglow emission layer at an altitude of ~82 km, over an ~2-hr interval (~10:30–12:30 UT), during strong eastward winds at the OH altitude and above, which weakened with time. The MWs displayed dominant horizontal wavelengths ranging from ~40 to 70 km and temperature perturbation amplitudes as large as ~35 K. The waves were characterized by an unusual, "saw-tooth" pattern in the larger-scale temperature field exhibiting narrow cold phases separating much broader warm phases with increasing temperatures toward the east, indicative of strong overturning and instability development. Estimates of the momentum fluxes during this event revealed a distinct periodicity (~25 min) with three well-defined peaks ranging from ~600 to 800 m^2/s^2, among the largest ever inferred at these altitudes. These results suggest that MW forcing at small horizontal scales (<100 km) can play large roles in the momentum budget of the mesopause region when forcing and propagation conditions allow them to reach mesospheric altitudes with large amplitudes. A detailed analysis of the instability dynamics accompanying this breaking MW event is presented in a companion paper, Fritts et al. (2019, https://doi.org/10.1029/2019jd030899).

1. Introduction

The Deep Propagating Gravity Wave Experiment (DEEPWAVE) was a highly successful combined airborne and ground-based measurement program conducted primarily over the New Zealand South Island and the surrounding oceans. The airborne flight program involved the National Science Foundation/National Center for Atmospheric Research Gulfstream V aircraft and the German Aerospace Center (DLR) Falcon aircraft and extended from 6 June to 21 July 2014. Clustered ground-based optical instruments operating concurrently from South Island (SI) obtained important additional observations complementing the flight program. DEEPWAVE differed from other gravity wave (GW) measurement programs in several respects. It was the first airborne program to quantify general GW fields from the surface almost continuously in altitude into the mesosphere and lower thermosphere (MLT) region (~80–100 km). It also enabled novel quantification of GWs, especially mountain waves (MWs), and their horizontal scales, vertical evolution, extension in altitude into the MLT, and temporal variability. An overview of the DEEPWAVE program, including weather forecasting, modeling support, flight planning and operations, airborne, ground-based, and satellite observations, and initial results is given by Fritts, Smith, et al. (2016).

There were many motivations for the DEEPWAVE measurement program. GWs are now known to play major roles in atmospheric dynamics from the Earth's surface into the MLT. However, many GW influences on atmospheric circulation, structure, and variability are poorly understood and consequently are not well described in large-scale models at present. At lower altitudes, significant GW effects include downslope windstorms (Durran, 1990; Klemp & Lilly, 1978), influences on convection and precipitation (Bougeault et al., 2001), and systematic weakening of eastward flows due to MW drag (McFarlane, 1987; Palmer et al., 1986). Importantly, GW transport of energy and momentum plays increasing roles at higher altitudes. Momentum deposition accompanying GW dissipation in varying mean winds contributes to the reversal of the mesospheric jets and induces a residual circulation having strong influences on thermal structures in the stratosphere and MLT at higher latitudes (Dunkerton, 1997; Dunkerton & Butchart, 1984; Fritts & Alexander, 2003; Garcia & Solomon, 1985; Holton, 1982; Lindzen, 1981; McLandress et al., 2012). GWs also exhibit strong interactions with tidal and planetary wave motions that can alter their amplitudes and vertical structure and map their horizontal structures to higher altitudes (Fritts & Vincent, 1987; Holton, 1984; Ortland & Alexander, 2006; Smith, 2003). Despite our advancing understanding of GW effects at lower and higher altitudes, there remain major unknowns regarding the relative roles of different GW sources. As an example of high relevance to DEEPWAVE, the GW sources expected to contribute "missing" momentum fluxes and drag that would alleviate the "cold pole" problem of the southern polar winter vortex in global models are believed to include orographic and frontal/jet-stream GW forcing (Alexander & Grimsdell, 2013; Hendricks et al., 2014; McLandress et al., 2012). While the sources, GW scales, propagation, and effects remain to be quantified, DEEPWAVE results have already demonstrated the importance of small islands in generating large momentum fluxes in the MLT over the Southern Ocean (Broutman et al., 2017; Eckermann et al., 2016; Pautet et al., 2016).

Many processes influence the vertical propagation of GWs and the evolution of the GW spectrum with increasing altitude. GW instabilities, especially wave breaking and Kelvin-Helmholtz shear instability, induced by increasing amplitudes and/or varying wind and stability profiles, can erode GW amplitudes (e.g., Fritts et al., 2009a; Fritts & Rastogi, 1985; Lilly & Kennedy, 1973; Lombard & Riley, 1996; Sonmor & Klaassen, 1997; Yamada et al., 2001). Multiscale superposition of GWs and larger-scale flows also yield strong wave-wave and wave/mean-flow interactions and various local instabilities that constrain GW amplitudes and drive strong spectral evolutions (e.g., Fritts et al., 2013, 2014; Fritts, Wang, et al., 2016; Smith et al., 2008). An important component of GW spectral evolution with increasing altitude is local momentum deposition that results in generation of secondary GWs that may propagate to much higher altitudes (Vadas & Fritts, 2002; Vadas & Liu, 2009).

The presence of GW "hot spots" exhibiting strong maxima in stratospheric temperature variances suggests sites of enhanced GW forcing due to strong convection at lower latitudes (e.g., Hocke & Tsuda, 2001; Jiang, Wang, et al., 2004; Stephan et al., 2019) and to airflow over significant terrain (e.g., Hoffmann et al., 2013; Jiang, Eckermann, et al., 2004) and potentially enhanced frontal activity and jet streams, at higher latitudes (e.g., Hendricks et al., 2014; McLandress et al., 2012). New Zealand is well known for its MWs when strong southeastward tropospheric winds impinge on the NE-SW aligned Southern Alps (see Figure 1). Such "Norwester" winds are common, especially during the winter months, when they can create stationary long white clouds suspended over the mountain range. This prominent MW phenomenon gives rise to the Maori name "Aotearoa" for New Zealand, which literally means "long white cloud." The hot spot extending over SI and the surrounding oceans (Jiang et al., 2003) was selected as the site for the DEEPWAVE field program.

To date, the majority of the DEEPWAVE analysis efforts have focused on specific research flights, given the unique and comprehensive nature of these data (e.g., Bossert et al., 2015, 2017; Eckermann et al., 2016; Heale et al., 2017; Pautet et al., 2016). However, there were a number of occasions when the aircraft did not fly as the lower atmosphere forcing was predicted to be weak. The night of 21 June was one such occasion where good prevailing weather conditions enabled high-quality extended observations by the ground-based instruments revealing dramatic MW responses in the MLT (Fritts, Smith, et al., 2016). This paper describes the evolution of this spectacular MW event and the observed MW scales, amplitudes, and momentum fluxes. A detailed analysis of the prominent instability dynamics generated by this strong breaking MW event is presented in a companion paper by Fritts et al. (2019), hereafter referred to as (*F19*).

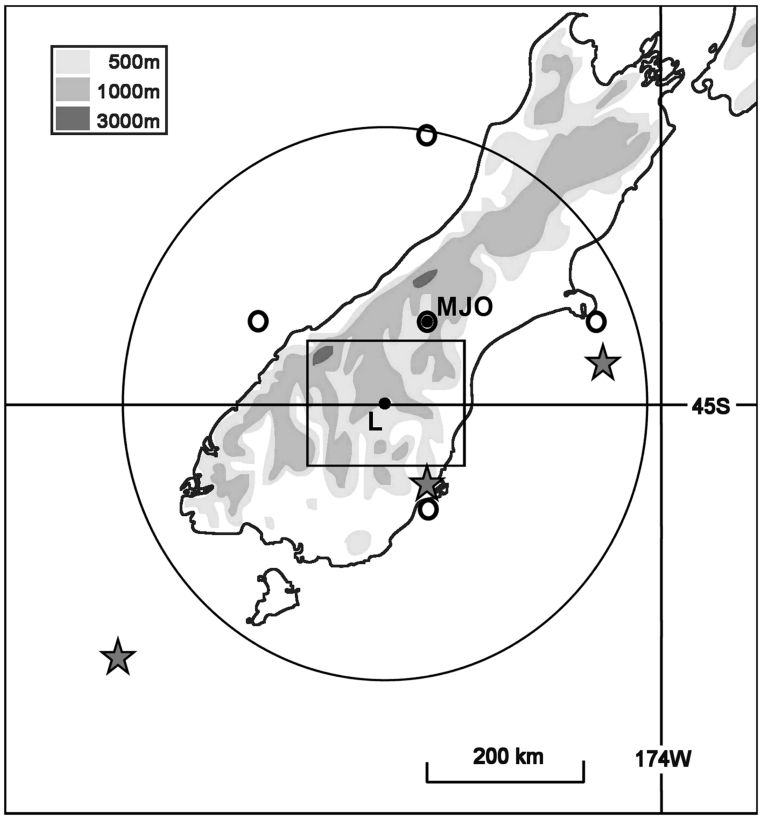

Figure 1. Contour map of New Zealand South Island identifying the extensive Southern Alps mountain range (terrain heights at 0.5, 1.0, and 3.0 km), and the locations of the optical sites at Lauder (L) and Mount John Observatory (MJO). The nominal fields of view of the Advanced Mesospheric Temperature Mapper (200 × 160-km rectangle) and the colocated all-sky imager at Lauder (~670-km diameter circle) are also shown. The five circles indicate the locations of the zenith, north, south, west, and east OH measurements by the Fabry-Perot Interferometer, while the three stars denote the locations of OH layer measurements obtained by Sounding of the Atmosphere using Broadband Emission Radiometry during the mountain wave event.

2. Ground-Based Sites, Instrumentation and Model

The New Zealand National Institute of Water and Atmospheric Research (NIWA) Observatory is located at Lauder (45.04°S, 169.68°E) in Central Otago, on SI. It is a well-established research station situated in the lee of the Southern Alps mountain range and is well known for its high-quality seeing conditions and geographical isolation (Liley & Forgan, 2009). Figure 1 shows a relief map of the South Island identifying the locations of Lauder (L) and Mount John Observatory (MJO, 45.72°S, 170.40°E), and their close proximity to the Southern Alps. As part of the DEEPWAVE collaborative program, NIWA hosted three remote sensing instruments at Lauder: a medium field Advanced Mesospheric Temperature Mapper (AMTM, Utah State University, USU), a zenith pointing Rayleigh lidar (German Aerospace Center, DLR), and an all-sky charge-coupled device imager (ASI, Boston University, BU). The Lauder site also supported regular radiosonde launches by DLR throughout the DEEPWAVE campaign. The fields of view of the AMTM and the ASI at the OH emission layer altitude are indicated by the rectangle (200 × 160 km) and the larger colocated circle (~670-km diameter), respectively. The small circles identify the locations of the north, south, west, and east OH measurements by the Fabry-Perot interferometer (FPI) operated by the University of Washington at Mount John Observatory (MJO). The map also plots the terrain contours at 0.5, 1.0, and 3.0 km identifying the broad backbone of the Southern Alps ranging along the length of SI.

The AMTM and ASI instruments were both set up under viewing domes within the observatory in May 2014. These instruments and the established FPI at MJO operated autonomously for the duration of the mission (30 May to 21 July). The mobile Rayleigh lidar system was set up at Lauder in mid-June and was operated

manually from its own container until November 2014. The three stars in Figure 1 also indicate tangent point locations at 90-km altitude for the SABER (Sounding of the Atmosphere using Broadband Emission Radiometry) OH profile measurements from the National Aeronautics and Space Administration (NASA) TIMED (Thermosphere Ionosphere Mesosphere Energy and Dynamics) satellite as it transited just to the south of NZ on the night of 21 June. Together, these measurements have enabled a detailed characterization of the GWs to quantify their horizontal wave properties, including their spatial extent, and temporal evolution, primarily at the OH emission altitude, and to measure directly their vertical structure, temperature amplitudes, and momentum fluxes as they propagated upward into the MLT region.

2.1. Advanced Mesospheric Temperature Mapper

The AMTM is a high-performance infrared digital imaging system developed at USU to quantify the structure, amplitudes and dynamics of GWs as they propagate through the OH layer (e.g., Bossert et al., 2015, 2017; Fritts et al., 2014, 2018; Pautet et al., 2016, 2018; Yuan et al., 2014). A fast telecentric lens system coupled to a sensitive cooled InGaAs (320 × 256 pixels) array enabled observations of the strong OH (3,1) band at ~1.55 μm, yielding an exceptional capability to measure a broad spectrum of gravity waves with periods ranging from several minutes to many hours.

For the DEEPWAVE mission, two AMTMs were employed: a newly developed system for operation on the Gulfstream V aircraft (Pautet et al., 2016) and a standard 120° field-of-view (FOV) ground-based system at Lauder. Both instruments sequentially measured selected emission lines in the OH (3,1) band and a nearby background. OH rotational temperature maps were determined using the line-pair-ratio method introduced by Meriwether (1975), and modified for the OH (3,1) band. For the ground-based system an exposure time of 10 s/filter was used resulting in a uniform time series of band intensity and temperature maps (~200 × 160 km) every ~30 s, with a zenith spatial resolution of 0.625 km/pixel.

Both AMTMs were cross calibrated at USU using observations alongside a well-established Na wind-temperature lidar, yielding similar temperature precision (~2 K/pixel) and an accuracy of ~5 K with respect to coincident height-weighted (full width, half maximum, FWHM ~8 km) lidar measurements using a nominal mean altitude of 87 km. For further details of the AMTM instrument and data processing see Pautet et al. (2014).

2.2. Rayleigh Lidar

TELMA (Temperature Lidar for Middle Atmosphere Research) is a powerful mobile Rayleigh-/Raman lidar system developed by DLR. A diode-pumped laser emitted 12 W of optical power at 532 nm with a 100-Hz pulse repetition frequency. Backscattered light was collected using an f/2.4 telescope with a 0.63-m aperture and a 240-μrad zenith field of view. The fiber-coupled receiver comprised three detectors operated in single photon counting mode, low- and high-rate channels for elastic scattering, and a 608-nm vibrational Raman channel. Note that the Raman channel was used only for data below 30 km and are not presented in this analysis. Detected photons were digitized with 2-ns temporal resolution relative to the laser pulse. The high temporal resolution allowed for flexible vertical and temporal binning of the photon count profiles during data analysis. TELMA was operated nightly from Lauder, weather permitting (Kaifler et al., 2015).

Data analysis involved initial binning of the raw photon data to a 100 m (vertical) by 10-min grid, in order to increase the signal-to-noise ratio. The resulting photon count profiles were then smoothed to 1,100 m × 10 min using a running mean filter. Assuming hydrostatic equilibrium, temperature profiles were retrieved separately for the two vertical resolutions using "top-down" integration of the range-corrected photon count profile, starting with the nightly mean profile, which was seeded with available TIMED/SABER overpass temperature profile measurements. The temporal resolution was subsequently enhanced in steps of 60-, 30-, 15-, and 10-min profiles. In each iteration, the seed temperature was obtained from the previous profile with coarser temporal resolution. GW temperature perturbations were calculated from the retrieved temperature profiles by subtraction of estimated undisturbed background profiles. The background profiles were obtained by filtering the retrieved profiles with a fifth-order Butterworth low-pass filter with a cutoff wavelength of 15 km (Ehard et al., 2015). For the 21 June MW event investigated herein, we used lidar temperature profiles with a vertical resolution of 1,100 m and integration times of 10 min to maximize sensitivity to the evolving wave field. Examples of the temperature perturbation profiles showing the vertical wave structure at three key times during the course of this event are shown in Figure 9.

2.3. All-Sky Multiwavelength Imager

For the DEEPWAVE program, BU installed a multiwavelength ASI at Lauder to sequentially observe four MLT airglow emissions on a nightly basis: the OH (~87 km), Na (~90 km), O_2 (~94 km), and O(^{1}S) (~96 km), where the parentheses indicate nominal layer altitudes. This imager utilized a 30 mm f/3.5 fish-eye lens system and a 1,024 × 1024-pixel back-illuminated bare CCD array, cooled to −60 °C. The 180° field of view enabled simultaneous monitoring of a large geographic area (>350,000 km^2) encompassing most of SI and extending over the surrounding oceans (see Figure 1). The ASI operated autonomously, sequentially observing each filter using a 120-s integration time, except for the broader-band OH emission, where a 30-s exposure was used. As a result, each nightglow emission was sampled every ~8–10 min providing information on the large-scale wave field at several MLT heights.

The raw images were processed using standard image reduction procedures, which involved dark subtraction, followed by flat fielding to remove lens vignetting and atmospheric viewing effects (e.g., Baumgardner et al., 2007). The images were further processed to remove stars and to reduce obscuring effects of the Milky Way and then mapped into geographic coordinates using their nominal emission altitudes or their measured altitude (as in this study for the OH emission).

2.4. Fabry-Perot Interferometer

A University of Washington FPI has operated at MJO since 1991, measuring horizontal winds in the MLT using selected airglow emissions (e.g., Hernandez & Smith, 1995). Here we describe the primary operation of the FPI during the DEEPWAVE mission. The interferometer collected light from a 1° half-angle field of view that was sequentially aimed north, south, east, and west, at 20° elevation and at the zenith (see Figure 1). The temperature-stabilized etalon was scanned using an electro-optical feedback system that maintained parallelism and accurately stepped the distance between the reflective surfaces (Hernandez & Mills, 1973). Light transmitted through the etalon was split into two wavelength bands, with each beam passing through a narrow (0.4–0.6 nm) interference filter, and was finally detected by two chilled GaAs photomultipliers. Single photons were counted until the scan profiles had accumulated sufficient photon counts, typically requiring a few minutes per look direction. A frequency stabilized HeNe laser provided the calibration light enabling accurate tracking of instrumental contributions and any frequency drift from zero (Conner et al., 1993).

For analysis, each accumulated scan was fitted to a model of an ideal instrument looking at a thermally broadened and Doppler-shifted line (Hernandez & McCarthy, 2011). A zero velocity Doppler shift was determined by averaging the fringe position when viewing the zenith over many clear days. The fringe shifts in the OH data were then scaled to line-of-sight speed and converted to horizontal wind speed, assuming vertical motion is zero. During the DEEPWAVE mission the FPI observed the $P_1(2)$ line of the OH (6,2) band, providing wind measurements at typically a 5-min cadence. These were averaged using a 3-point smoothing, providing wind measurements every ~15 min. Measurement uncertainties, due primarily to Poisson statistics in the accumulated scans, yielded an uncertainty of ~ ±4 m/s for the averaged data.

2.5. SABER Instrument

The OH nightglow is one of the most studied airglow emissions, originating in the upper mesosphere, and exhibits a well-defined peak at a nominal altitude of ~87 km and a FWHM of ~8 km (Baker & Stair, 1988). However, satellite and ground-based studies have also revealed significant variability in the peak altitude of the OH nightglow emission, by up to several kilometers, depending on latitude and season, as well as local time, due mainly to large-scale atmospheric tides (e.g., Mulligan et al., 2009; von Savigny et al., 2012; Zhao et al., 2005). For this investigation we have used near coincident opportune 1.6-μm OH channel data obtained by the SABER instrument on the NASA TIMED satellite to determine peak height and thickness (FWHM) of the OH emission layer and also to provide initial reference temperature profiles to aid the Rayleigh lidar data analysis.

2.6. NAVGEM Model

The US Navy Global Environmental Model (NAVGEM) is an operational global numerical weather prediction system that couples a forecast model to a hybrid four-dimensional variational data assimilation algorithm. NAVGEM assimilates >3 million observations from ground-based, suborbital and satellite

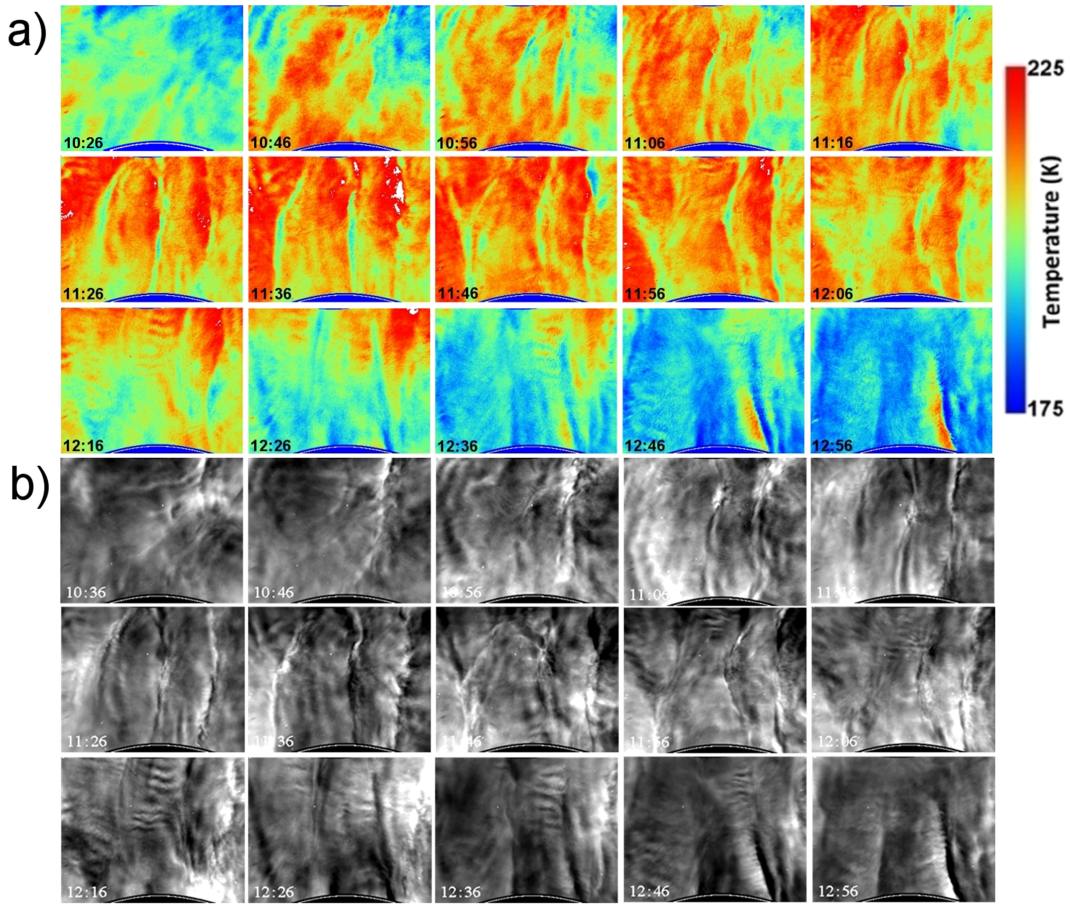

Figure 2. (a) Time series "mosaic" of OH rotational temperature maps (top, color) and corresponding $P_1(2)$ intensity images (bottom, grayscale), capturing the rapid growth and structure of an intense, quasi-stationary mountain wave (MW) and its dissipation. Images selected at regular ~10-min intervals encompassing the primary period of the MW event from 10:26 to 12:56 UT (except for the first pair of color images, which have a 20-min interval). Note that the temperature data are all plotted on the same scale to facilitate direct comparison while the intensity images have each been normalized to more clearly show the complex constituent MW structures and their evolution.

platforms every 6 hr (Hogan et al., 2014). A high-altitude NAVGEM extending to ~110 km that assimilates satellite data above 50-km altitude was developed (Hoppel et al., 2013) and recently validated during DEEPWAVE (Eckermann et al., 2016). For the night of 21 June, NAVGEM assimilated results of the zonal winds were used over a geographic region (between 43–47.5°S and 166–173°W), encompassing the southern SI ground-based and SABER observations.

3. Observations and Results

The sources of the MWs are strong wind forcing over prominent orographic features such as mountain ranges. They are naturally formed in the lee of the mountains and appear near parallel to the mountain ridges (e.g., Smith et al., 2009). During the winter months, MWs can penetrate into the upper mesosphere when the zero wind line (a critical level for MWs) is expected to lie above 90 km (see F19). A most important signature of MWs is their near zero observed horizontal phase speeds (quasi-stationary), while most GWs exhibit substantial horizontal phase speeds (typically a few 10 m/s to >100 m/s, e.g., Taylor et al., 1997).

Initial joint ASI and AMTM observations were made from Lauder on 30 May and revealed several well-defined GW events during the course of the night, including a quasi-stationary mesospheric MW event toward the end of the night that exhibited near zero ground relative phase speed. The characteristics and

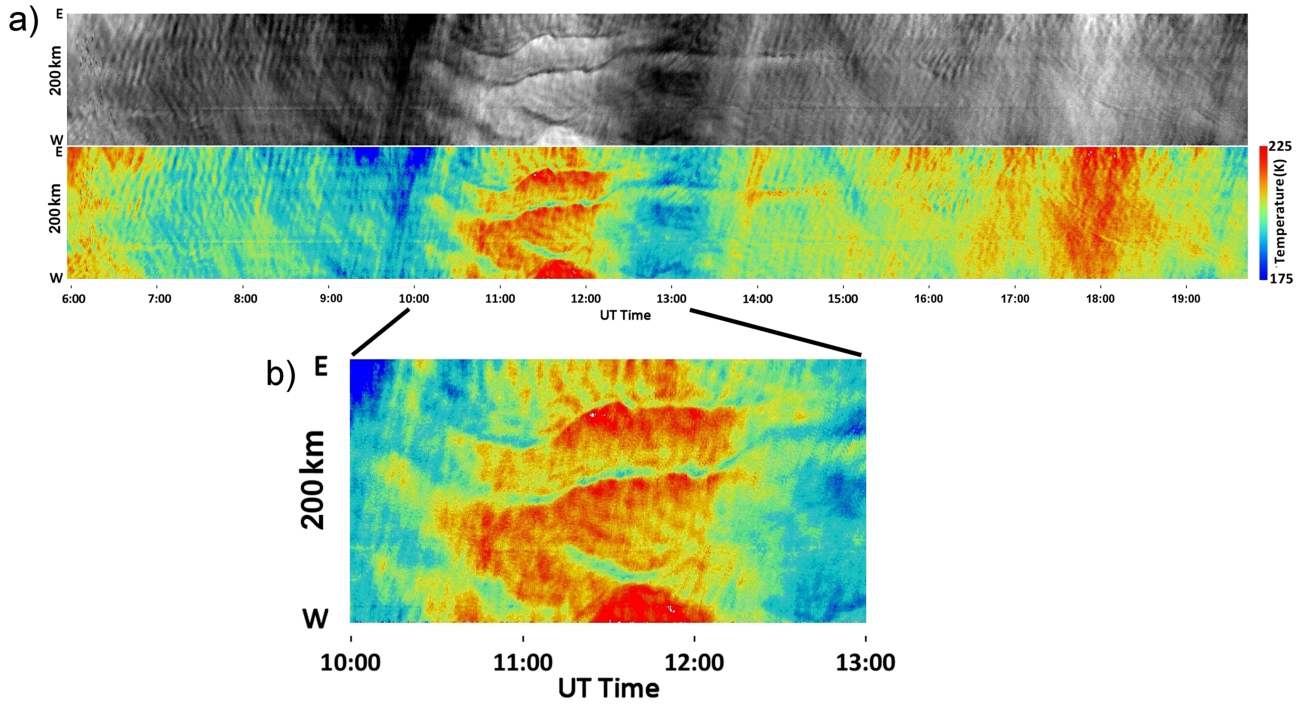

Figure 3. E-W keogram plot summarizing wave activity in the OH (3,1) band intensity (a) and rotational temperature (b) over Lauder for 21 June 2014. Note the sudden onset of strong wave activity around ~10:30 UT (duration ~3 hr) appearing as a rapid concurrent increase in the OH intensity and temperature structures. The enlargement reveals three bright near-horizontally aligned (in time) broad warm phases separated by narrow cold phases, characterizing the development of this unusual quasi-stationary mesospheric mountain wave event. Also note the subsequent faint, lingering horizontal tails in both the intensity and temperature keograms associated with continued localized mountain wave breaking to ~15:00 UT (see F19).

behavior of this latter event on 30 May was typical for MWs. These observations set the scene for the DEEPWAVE campaign and nightly measurements were made over the next 6 weeks resulting in the detection of MW signatures on 28 nights out of a total of 40 clear or partially clear nights. These novel MW observations provided high-quality data on their dominant signatures and temperature amplitudes in the MLT. The MWs were observed with varying durations; some persisted throughout the entire night, while others were only partially detected due to clouds. However, as with the 21 June event investigated herein, most MWs occurred as isolated outbreaks of wave activity, typically lasting for only a few hours (McLaughlin, 2018). In the following sections, the joint measurements on 21 June are used to investigate the temporal development and scales of this large MW event, focusing on its remarkable temperature and intensity structure and evolution.

3.1. June 21 Mountain Wave Event

The seeing conditions throughout this night were excellent, and a spectacular outburst of unusual mesospheric MW activity was observed over SI for a limited ~2.5-hr period (~10:30–13:00 UT). Observations were most prominent in the AMTM OH temperature and intensity data. Figure 2 depicts the structural evolution of this event in a time series of 15 temperature maps (a) and corresponding OH $P_1(2)$ intensity images (b), focusing on the main period. The temperature images are all plotted with the same temperature scale to facilitate direct comparison, while the intensity images have each been normalized to reveal the intricate MW structure and its evolution. Note that the first temperature image in Figure 2 shows the background temperature field at 10:26 UT just prior to the onset of the event, while the corresponding intensity image shows the beginning of the event ~10 min later. Subsequent temperature and intensity image pairs are shown at ~10-min intervals. A summary view of Figure 2 shows that over Lauder, this mesospheric event appeared as a set of quasi-stationary ~N-S aligned broad structures exhibiting large OH intensity and temperature perturbations, which were observed to form, grow, and dissipate. These unusual structures appear as periodic "broad warm phases" separated by pronounced "narrow cold phases."

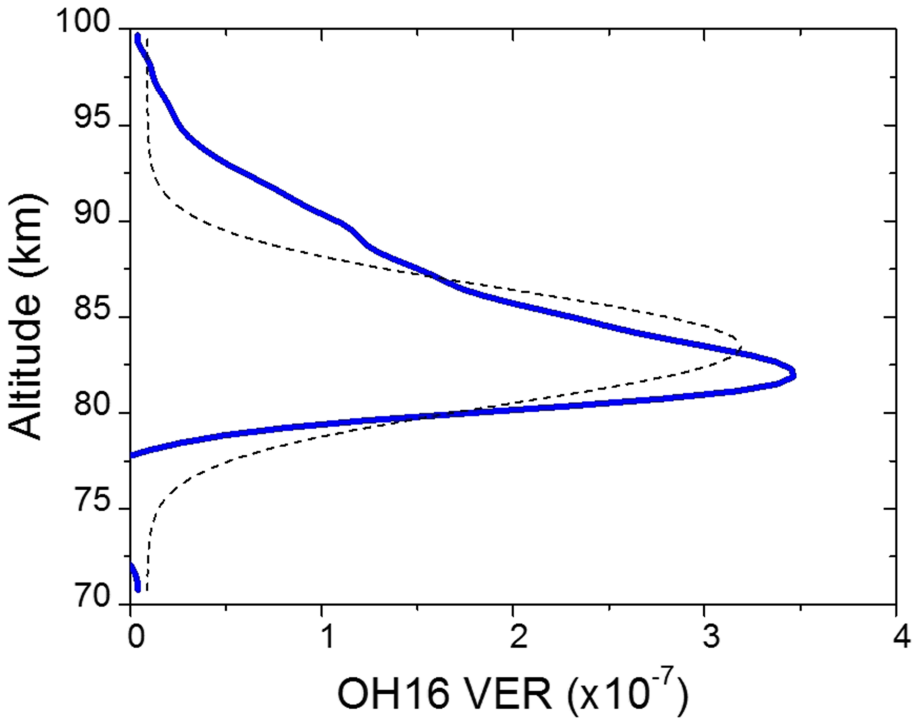

Figure 4. OH altitude profile as measured by Sounding of the Atmosphere using Broadband Emission Radiometry on the Thermosphere Ionosphere Mesosphere Energy and Dynamics satellite using the OH 1.6-μm band filter (OH_16_ver) as it transited to the south of New Zealand at 12:19:19 UT (Figure 1, central star) during the mountain wave event. The profile reveals a well-defined peak with a full width, half maximum of ~6.7 km, as determined by the Gaussian fit (dashed line). Applied corrections for the OH (3,1) band emission resulted in a mean layer height of ~82 ± 0.5 km, full width, half maximum ~7 km.

Close inspection of Figure 2a images also shows that the N-S aligned phase structures of the MW evolved significantly in time (top row), leading to three well-developed broad warm phases (red structures) separated by two distinct narrow cold phases (blue structures), which occurred near the zenith and to the west, with a third, less well-formed cold phase to the east after ~11:26 UT (center row). Subsequently, these structures filled the FOV of the AMTM and were observed to increase in intensity and temperature with time (center rows). These primary features remained coherent up until ~12:00 UT, after which they decayed rapidly in form and amplitude into a variety of complex wave breaking signatures (bottom row). The corresponding intensity data also reveal finer-scale east-west (E-W) aligned structures associated with this spectacular MW event. The ensuing instabilities continued to evolve and are discussed in detail in *F19*.

To place this event in broader context, the keogram plot of Figure 3 summarizes the mesospheric wave activity throughout this night (06:00–19:40 UT, duration ~13.7 hr) as recorded by the AMTM. Keograms are made by stacking together individual zonal (E-W) and meridional (N-S) scans through the centers of each image in the data sequence to create a compressed time history of the wave activity (e.g., Taylor et al., 2009). The ~N-S aligned MWs observed in Figure 2 exhibited near zero phase speed and therefore appear as quasi-horizontal structures in the E-W keogram (Smith et al., 2009), while propagating waves pass through the keogram at various angles. Figure 3a shows the E-W keograms for the OH band relative intensity (top) and temperature (bottom). The sudden onset of major MW activity in the OH layer (around ~10:30 UT) is depicted by the near horizontal structures that appeared as a rapid increase in both the OH band intensity and OH temperature above the prevailing relatively cool (T ~ 180 K) dark background. This event exhibited a peak in activity around 12:00 UT coinciding with a quasi-periodic warming evident in the temperature keogram, with additional peaks around 06 and 18 UT, indicating the presence of a large ~6-hr GW. The broad warm phases and narrow cold phases comprising this event are shown more clearly in the enlargement of the temperature keogram in Figure 3b and appear to be unique in our observational experience, differing markedly from the faint

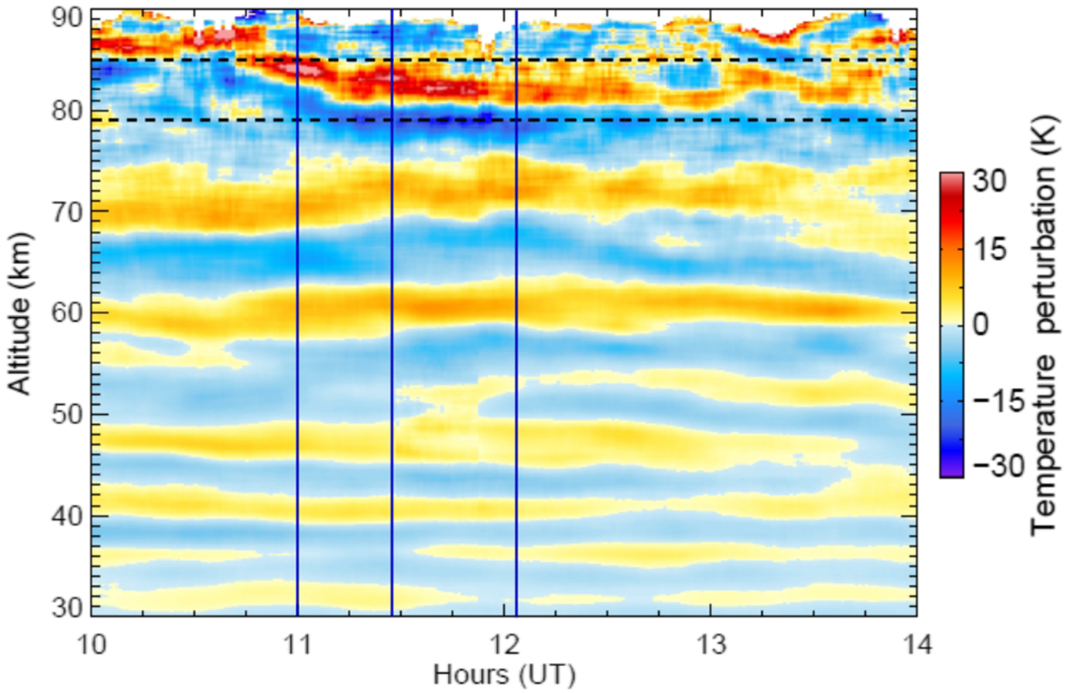

Figure 5. Summary Rayleigh lidar plot showing vertical temperature perturbation structure from 30 to ~90 km over a 4-hr period (10:00–14:00 UT) encompassing the mountain wave event. The 15-min averaged data reveal a series of coherent temporarily extensive, near-horizontal mountain wave crests dominating the middle atmosphere. The color bar shows the temperature perturbations increasing with altitude, with largest amplitudes (red) occurring over the same altitude range as the OH layer ±3 km (horizontal dashed line). The three vertical lines identify the times of individual profiles presented in Figure 9.

near-continuous fine-scale ducted (and chaotic) type waves that were also evident in the keogram during most of this night.

A time lapse temperature movie showing the development of this MW event over a 4-hr period (10:00–14:00 UT), encompassing the OH activity before, during, and after this spectacular MW event, is also provided (AMTM_T.mp4, links in the supporting informationsupporting information) to further aid the readers' comprehension. The movie shows the derived temperature maps obtained with a ~30-s cadence. For viewing, the movie has been speeded up by a factor of 330.

3.2. Complementary Observations

On 21 June the SABER instrument on the TIMED satellite transited to the south of NZ at ~12:18 UT. The three black stars in Figure 1 represent the geographic location of the SABER measurements (90-km tangent height), establishing the high spatial and temporal coincidence with this MW event. Three consecutive measurements of the OH emission profile using the 1.6-μm channel (OH_16_ver) were obtained over the next 3 min. Figure 4 plots the central OH profile measurement (12:19:19 UT) that overlapped best with our ground-based viewing fields. This and the subsequent profile at 12:20:01 UT (not shown) were almost identical in shape, establishing the OH layer peak at an altitude of 82–82.5 km, and a FWHM layer thickness of 6.7 km, as estimated by the Gaussian fit (dashed line). The earlier profile (12:18:09 UT), furthest to the southwest of the SI, exhibited a somewhat broader emission profile of ~10 km FWHM, but a similar peak emission altitude of ~83 km. As the SABER 1.6-μm channel measurements comprise emissions primarily from the OH (4,2) and (5,3) bands, a small correction was necessary to account for expected differences in altitude between these layers/bands and the OH (3,1) band (von Savigny et al., 2012). This resulted in a corrected mean peak height of ~82 ± 0.5 km (with a FWHM ~7.0 km), significantly lower than its nominal altitude.

Complementary colocated Rayleigh lidar observations were made from Lauder throughout this night. Figure 5 summarizes the derived vertical temperature perturbation structure over a 4-hr period (10:00–

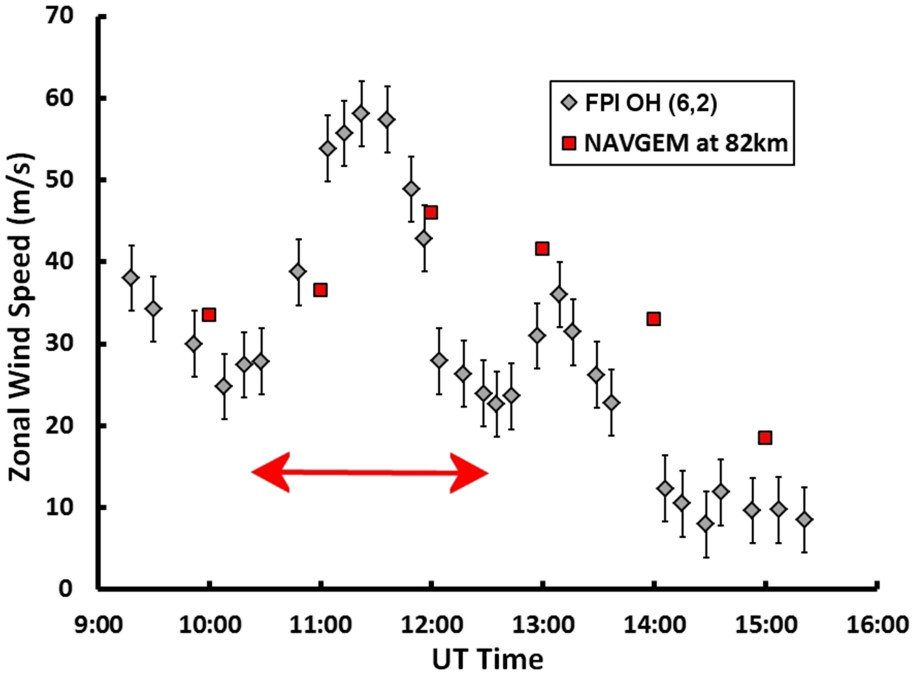

Figure 6. Plots the zonal wind field and its temporal variability during a ~6-hr period encompassing the mountain wave event. The measurements were made by the Fabry-Perot interferometer (FPI) observing the OH (6,2) band, from Mount John Observatory (see Figure 1). The 15-min averaged zonal measurements (diamonds) reveal persistent eastward flow throughout the night that rapidly increased to over 60 m/s during the mountain wave event. For comparison, the solid squares plot the Navy Global Environmental Model (NAVGEM) reanalysis of the wind field at ~82 km. Both data sets track the increase in the zonal wind field prior to ~12:00 UT and the subsequent reduction during the rest of the night.

14:00 UT) encompassing the MW event, as a function of altitude (from 30 to ~90 km). The 15-min averaged data reveal a series of coherent temporarily extensive, near-horizontal MW oscillations, dominating the middle atmosphere. The colors show the MW temperature perturbations increasing with altitude, with largest amplitudes (~35 K) occurring over the same altitude range as the observed OH layer at ~82 km. The dashed horizontal lines at ±3 km centered on the OH layer represent its FWHM and are used to guide the eye in the following discussion. Close inspection of this plot shows that around 10:30 UT the MW penetrated up to ~85 km where it was suddenly observed as a rapid growth in MW activity in the OH imagery (centered at ~82 km, as depicted in Figures 2 and 3). Note that earlier this night the lidar data showed only incoherent MW activity (see Figure 2a in *F19*). During the next 1.5 hr (~11:00–12:30 UT), the MW event remained prominent and coherent, penetrating up to and including the OH layer, where it exhibited large temperature perturbations. Thereafter, the amplitude of the MW began to decrease, and its coherence reduced significantly.

During the DEEPWAVE campaign, mesospheric wind measurements were also made by a FPI observing the OH (6,2) band, from MJO located ~130 km to the northeast of Lauder (see Figure 1). Figure 6 plots the zonal wind field and its temporal variability during a ~6-hr interval (~09:15–15:30 UT) encompassing the MW event. The averaged (15 min) zonal measurements (diamonds) reveal persistent eastward flow at the ~82-km level throughout the night. Prior to the onset of the event, the zonal wind was moderate and decreasing to ~25 m/s; however, around 10:30 UT, the wind rapidly increased, reaching a peak of ~60 m/s, where it remained uniformly high at >50 m/s until ~12:00 UT. Then followed a rapid reduction in the zonal winds to ~25 m/s (~12:30 UT). The MW event coincided with the period of strongly enhanced zonal wind from ~10:30–12:30 UT (as indicated by the red arrow).

In addition, Figure 6 also plots the hourly NAVGEM reanalysis wind field at ~82-km altitude (solid squares). These reanalysis data compare well with the observed FPI winds, tracking the initial increase in the zonal wind field prior to ~12:00 UT and the subsequent reduction in magnitude during the rest of the night. However, the NAVGEM data are not as sensitive to the local, smaller-scale changes present in the FPI

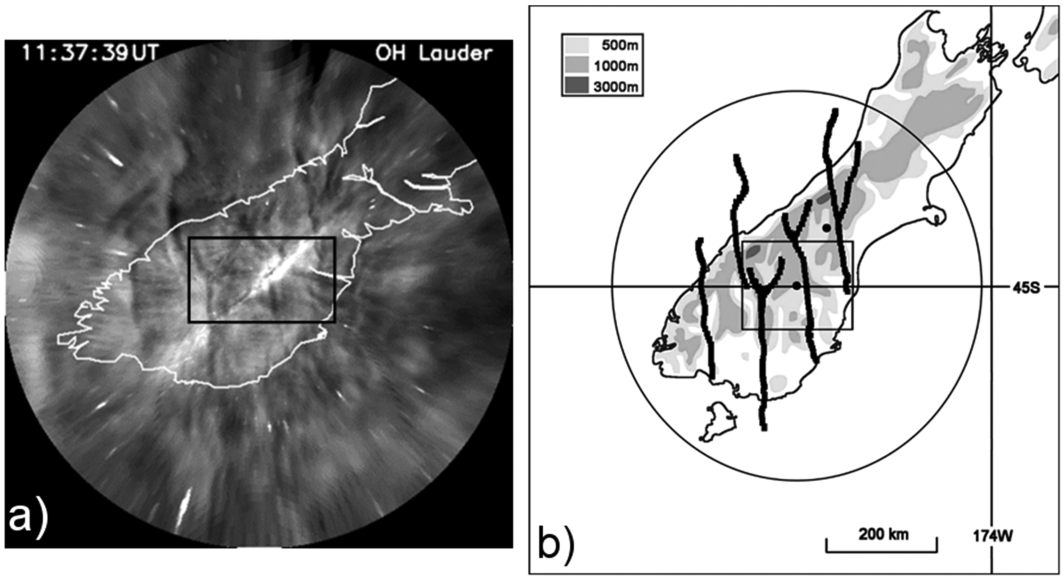

Figure 7. (a) Wide-field geographic mapping (~670-km diameter) of the OH all-sky data at 11:37 UT showing the larger-scale mountain wave structures. For reference the coastal outline of the South Island and the rectangular field of view of the Advanced Mesospheric Temperature Mapper (AMTM) are superimposed. (b) Sketch identifying the location and extent of four main ~N-S aligned mountain wave structures, three of which correspond with the narrow cold phases evident in the smaller field AMTM data (section 3.1 and Figure 2). Note that the bright SW-NE aligned luminous band in (a) is the projection of the Milky Way, and should be disregarded.

data. Nevertheless, these independent data sets provide high confidence establishing the prevailing strong eastward winds, supporting the propagation of the MWs into the upper mesosphere at this time. In particular, the NAVGEM zonal wind field established consistent eastward winds from ground to MLT altitudes during this event, which allowed the MW to propagate from its tropospheric source to the OH layer (see Figure 3 in *F19* for further details of the hourly vertical profiles). These complementary observations establish the spatial and temporal consistency of this MW event and its dominance at MLT altitudes during this period.

3.3. MW Geographic Extent

The regional extent of the MW event and its larger spatial scale have been estimated from the coaligned all-sky imagery. Figure 7a shows a wide-field mapping of the OH data at 11:37 UT, close to the peak time of the MW activity. The image has been processed and projected into geographic coordinates using 82-km altitude (as a best estimate for the OH emission layer altitude) and mapped onto a circular field of view of ~670-km diameter. For reference, the coastal outline of the SI and the rectangular FOV of the AMTM are superimposed.

Close examination of these data and the other observed airglow emissions (not shown) establishes that the main MW activity was centered over the southern SI and was characterized by four N-S aligned elongated "dark structures." For clarity, these structures are identified in Figure 7b, which sketches their location and extent (corresponding to the narrow cold phases evident in the smaller field AMTM data, as discussed in section 3.1). Furthermore, the wide-field data establish that all four structures extended coherently across SI but were strongest to the north and that at least two extended well to the north of NZ over the Tasman Sea and one to the south over the South Pacific Ocean, indicating a latitudinal extent >500 km (see Figure 7b sketch), while their longitudinal extent was more confined (to ~400 km). This suggests that the MW event had a large region of influence near the mesopause of >200,000 km^2.

3.4. MW Horizontal Characteristics

Figure 8a plots the AMTM OH temperature data at approximately the same time as the wide field intensity image of Figure 7a, providing a more detailed view of the dominant horizontal spatial scales and temperature perturbations characterizing the MW at this time. In particular, the temperature data define the zonal

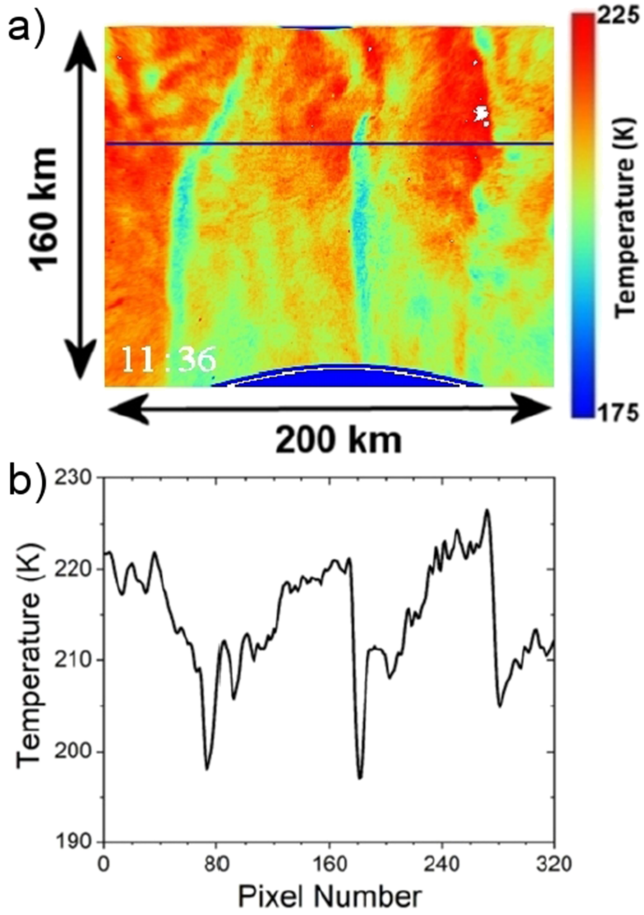

Figure 8. (a) Advanced Mesospheric Temperature Mapper temperature map at 11:36 UT illustrating the horizontal spatial scales and temperature structures characterizing two adjacent mountain wave cycles and (b) graph showing a horizontal cross section through the temperature map (indicated by the horizontal line) where the mountain wave event was well developed and most distinct. Note the narrow cold phases and broad warm phases comprising each cycle as well as the large temperature perturbations (−20–25 K) and the unusual periodic saw-tooth variation, as well as the finer-scale structuring within each warm phase.

structure of two adjacent MW cycles occurring overhead at Lauder. At this time the MW structures were warmer and their horizontal wavelengths were shorter to the north, and evolving during the development of the event (as shown in Figure 2a and the temperature movie).

To further investigate these cycles, Figure 8b plots an E-W scan through the temperature map (indicated by the horizontal line in Figure 8a) where the MW event was most distinct. This figure is characterized by two unusual periodic approximately "saw-tooth" variations in temperature (Fritts, Smith, et al., 2016). In particular, the narrow cold phases in each cycle were typically ~5- to 8-km wide and exhibited steep temperature drops (~20–25 K), while the associated broad warm phases were characterized by a temperature ramp, consistently warmer to the eastern side of its warm phase (by 10–15 K). Finer-scale wave structures were evident superposed on the warm phase of the MW. The horizontal widths of the two warm maxima were ~83 km (left) and ~62 km (right) at this time.

Average horizontal wavelengths using the zenith E-W scan for the central two saw-tooth cycles were found to vary from ~40 to 70 km during the course of the event (see Table 1). Similar zenith scans (not shown) taken at multiple times during this event establish the persistent saw-tooth structure in the temperature field as the primary MW signature. Importantly, this saw-tooth shape is a characteristic signature of an overturning gravity wave associated with wave breaking in more general flows (see *F19*).

3.5. MW Vertical Structure

The summary lidar data in Figure 5 introduced the vertical signature of the MW. To further investigate the vertical structure and wavelength of this event, Figure 9 plots three 10-min averaged lidar temperature perturbation T' profiles (black curves) at key times (11:00, 11:26, and 12:04 UT) during the main stage of this event (left column). For reference, the times of these three profiles are also plotted in Figure 5 by the vertical lines. Each of the three profiles in Figure 9 were obtained using a 1,100-m vertical resolution and clearly revealed the growth of the MW amplitude with altitude. The approximate location of the OH layer (79–85 km) is also indicated on each plot by the horizontal dashed lines. To further aid this comparison, the corresponding horizontal MW structures as measured by the AMTM are shown in the adjacent temperature maps for each lidar profile (right column). The black dot at the center of each map marks the zenith location of the lidar measurements. As noted earlier in Figure 5, the concurrence of the large amplitude MW crest with the OH layer is also evident. The figure clearly shows that during this key period the lidar fortuitously sampled the transition region between the narrow cold phase and eastern edge of the broad warm phase, where the temperature perturbations were largest. At 11:00 UT the lidar temperature in Figure 9a began to exhibit very large wave perturbations of >70 K peak to peak (~35 K amplitude), at the OH layer altitude. Approximately 25 min later (Figure 9b), the lidar continued to reveal sustained MW activity but with reduced amplitudes (25–33 K). By 12:05 UT (Figure 9c), the MW had begun to dissipate and the corresponding temperature amplitude had decreased further. Each lidar profile shows that below ~60 km, the wave amplitudes were relatively small, but above this altitude the MW phase structures were clearly coherent and exhibited vertical wavelengths of ~10–15 km that decreased with time. Together, these data provide direct measurements of the MW perturbation amplitudes and their horizontal and vertical wavelengths at the OH level, as well as their variability with time. Figure 10 plots the measured vertical wavelength λ_z using all the lidar profiles between 10:30 and 12:30 UT. During this period, λ_z decreased almost monotonically from an initial value of ~15 km down to ~8.7 km (an ~40% reduction). These results together with other key MW parameters are summarized in Table 1, which lists 12 selected times (out of a total of 41 measurements) spanning most of the

Table 1
Summary of MW Characteristics at 12 Selected Times During the Event, Determined Using the Joint Airglow and Lidar Measurements

Lidar		AMTM				
UT time	λz (km)	T′ (K)	λx (km)	T_0 (K)	T'/T_0	MF (m^2/s^2)
10:34	14.8	17.6	65.9	200	0.09	244
10:48	14.8	23.1	68.3	206	0.11	384
11:00	13.5	35.9	63.6	207	0.17	898
11:06	12.6	27.8	64.6	209	0.13	487
11:16	10.4	28.8	53.9	210	0.14	510
11:25	11.8	33.5	60.7	211	0.16	690
11:34	10.2	25.5	71.0	210	0.12	297
11:46	10.4	37.4	65.5	211	0.18	702
11:56	10.2	26.2	61.5	210	0.12	364
12:06	9.6	28	51.2	207	0.14	485
12:18	8.7	21.4	56.1	202	0.11	246
12:26	10.4	14.5	45.8	199	0.07	170
	$\Delta\lambda z = 0.5$ km	$\Delta T' = 5$ K	$\Delta\lambda x = 5$ km	$\Delta T0 = 5$ K		

Note. MW = mountain wave; AMTM = Advanced Mesospheric Temperature Mapper; MF = momentum flux.

event. These joint measurements have been used to investigate the temporal development and scales of this unusual MW event, focusing on its remarkable temperature and intensity structure and evolution. We now investigate the source of these MW and their potential impact on the MLT region.

4. Discussion

Mountain waves are a special case of upward propagating GWs. Under favorable background wind conditions, they may transport large amounts of momentum from the lower atmosphere into the MLT region (Fritts & Alexander, 2003). Initial radar studies (e.g., Vincent & Reid, 1983; Reid & Vincent, 1987; Nakamura et al., 1993) of momentum flux (MF), which is defined as $<u'w'>$ (where u' and w' are the horizontal and vertical wind perturbations and $< >$ denotes a spatial or temporal average over the GW phase), have indicated relatively small mean $< u'w' >$ at mesospheric heights of typically 5–10 m^2/s^2. Similarly, satellite observations of zonal MF averages have showed values of 2–3 m^2/s^2 in the mesopause region at 40°S during the Austral winter (Ern et al., 2018). However, following the first clear detection of a breaking GW event observed in the mesospheric OH airglow emission over Japan by Yamada et al. (2001), considerable attention has focused on estimating MFs associated with well-defined GW events. This is primarily because such breaking events have been connected with very large MF estimates (e.g., ~900 m^2/s^2 for the "Yamada event," Fritts et al., 2002). There were also many previous radar measurements of MFs, some of which also exhibited larger values, but none this large (Fritts & Alexander, 2003). Little is currently known of the MW amplitudes and their associated MFs at mesopause heights. A key goal of the DEEPWAVE mission was to identify distinct MW events and measure their MFs and potential impacts on the MLT region (Bossert et al., 2018; Eckermann et al., 2016; Fritts et al., 2018; Kaifler et al., 2015; Pautet et al., 2016). Our combined measurements of the 21 June event provide an exceptional resource for quantifying the MFs accompanying one very prominent MLT event and investigating its variability.

4.1. MW Momentum Flux and Variability

To investigate the variability of the MW amplitudes and MFs with time, Figure 11 plots the fractional temperature perturbation amplitude T'/T_o *as* measured during this event, where T' is the wave amplitude (measured directly from the Rayleigh lidar data) and T_0 is the zenith average background temperature (determined using the AMTM image data). The vertical bars depict the combined T'/T_0 uncertainty $\Delta(T'/T_0)$ given by

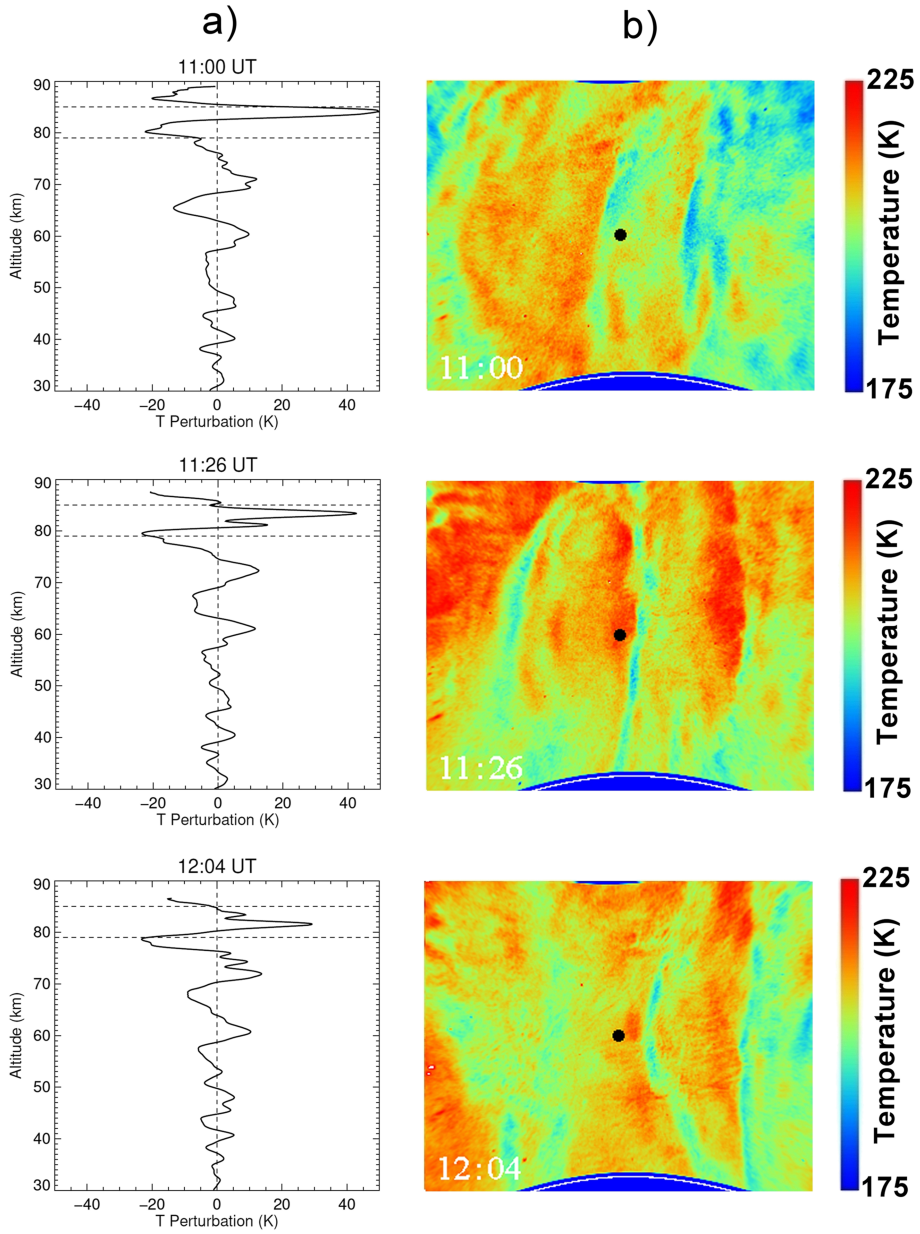

Figure 9. Three examples of 10-min averaged (1,100-m vertical resolution) lidar temperature perturbation profiles (black curves) at ~30 min intervals (11:00, 11:26, and 12:04 UT) during the main stage of the mountain wave (MW) event. Note that the coherent growth in amplitude of the MW with height and the favorable concurrence of the large amplitude MW with the OH layer (indicated by the dashed lines). The corresponding horizontal MW structures are shown in the adjacent temperature map. The black dot at the center of each map marks the location of the lidar measurements.

$$\Delta\left(\frac{T'}{T_0}\right) = \frac{1}{T_0}\sqrt{(\Delta T')^2 + (\Delta T_0)^2.\left(\frac{T'}{T_0}\right)^2} \quad (1)$$

where $\Delta T'$ and ΔT_0 are estimated to be 5 K.

The results reveal a quasi-periodic (~25 min) oscillation in T'/T_0 with three distinct peaks occurring around 11:00, 11:25, and 11:50 UT. When the MW event was first detected, the fractional temperature amplitude was already substantial (around 7%), subsequently T'/T_0 was observed to more than double (to >15%) at each of the three peaks, before decreasing to earlier levels around 12:30 UT.

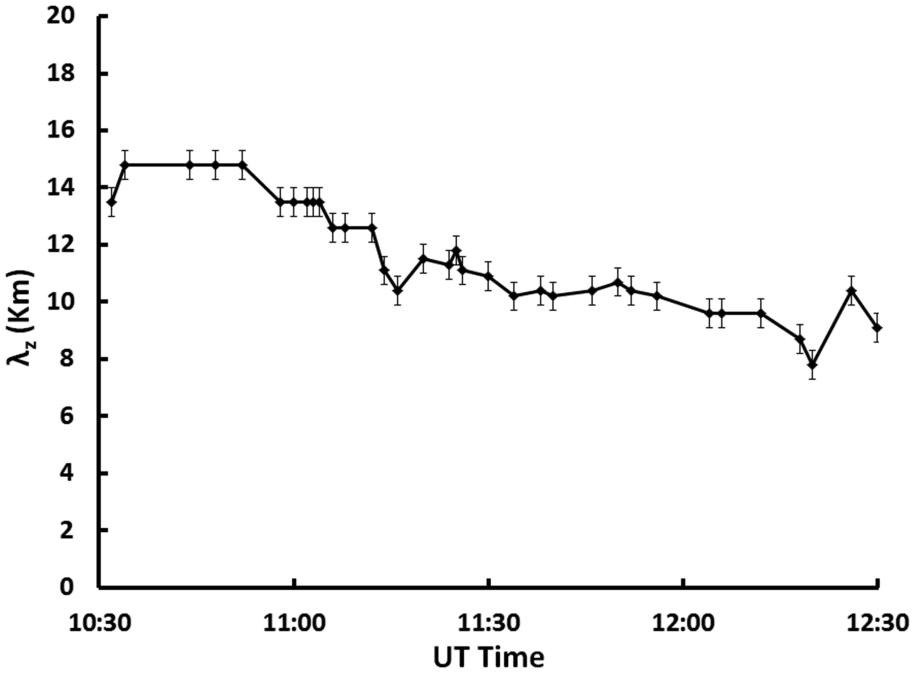

Figure 10. Plots Rayleigh lidar measurements of the vertical wavelength λ_z as a function of time. Note the steady reduction in λ_z from an initial value of ~15 km down to ~8.7 km. (~40%) during the ~2-hr mountain wave event.

Using the MW parameters measured by the AMTM and the Rayleigh lidar, the MF was calculated using the following equation (Alexander & Teitelbaum, 2007), which relies on the linear gravity wave polarization relations. (See F19 for further details.)

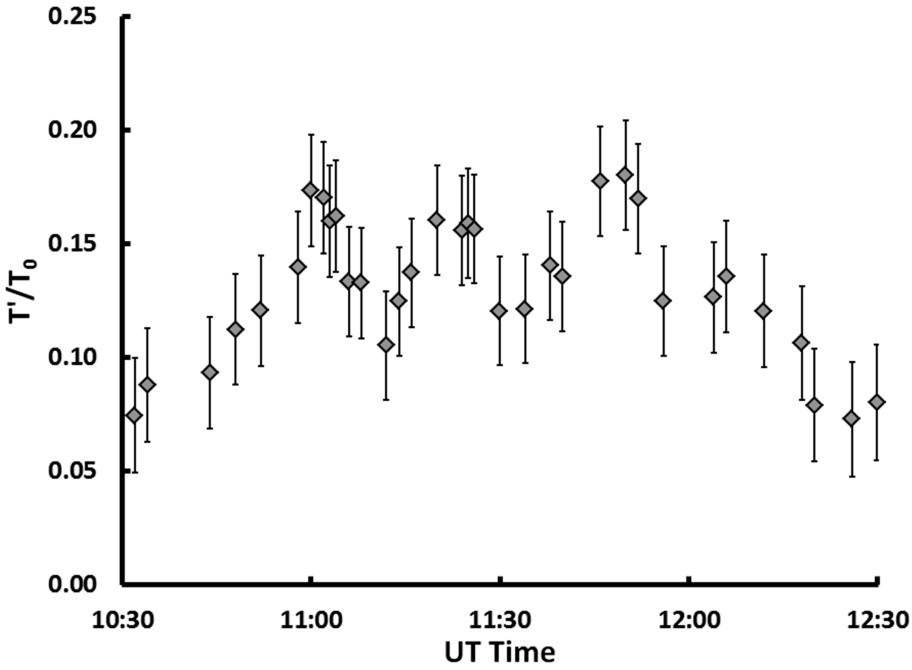

Figure 11. The fractional temperature perturbation amplitude T'/T_0 during the evolution of the mountain wave event where T' values were measured directly from the Rayleigh lidar profiles, while T_0 levels were determined from the Advanced Mesospheric Temperature Mapper temperature maps. Note the three distinct peaks (amplitudes ≥15%) occurring around 11:00, 11:25, and 11:50 UT with a quasi-periodicity of ~25 min.

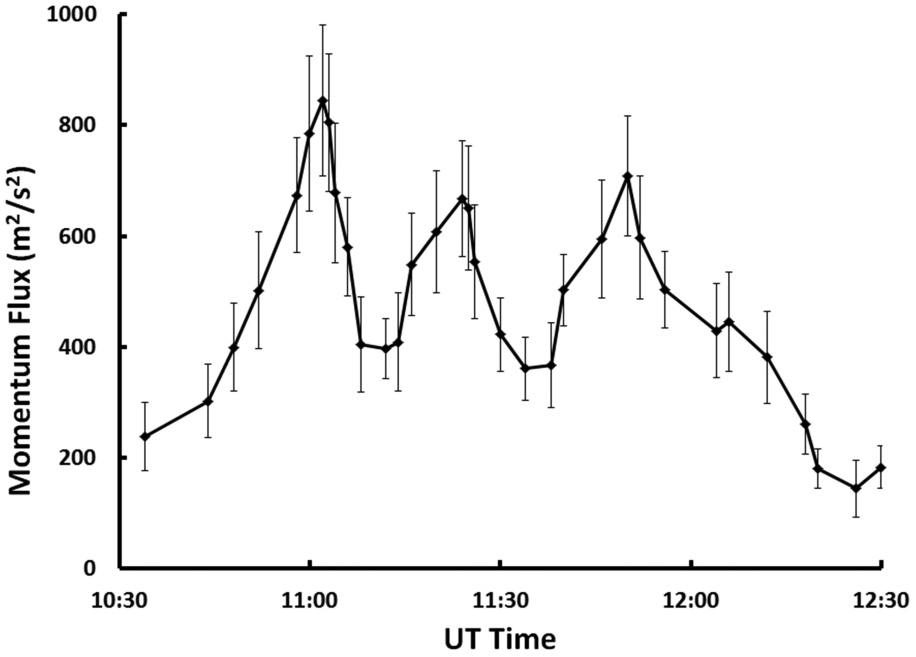

Figure 12. Plot of the derived momentum flux (MF) as a function of universal time (3-point averaged) using equations (2) and (3). Note the high level of sustained MFs and implied mesosphere and lower thermosphere forcing (>400 m^2/s^2) for most of the event. The three distinct peaks in MF exhibit magnitudes ranging from ~600 to 800 m^2/s^2 and are driven strongly by the large T'/T_0 perturbations in Figure 11. As noted in F19 the occurrences of strong instability dynamics associated with this breaking mountain wave event appears to correlate well with the minima in the mountain wave MFs shown in this figure.

$$<u'w'> = \frac{1}{2}\frac{g^2}{N^2}\frac{\lambda_z}{\lambda_x}\left(\frac{T'}{T_0}\right)^2 \tag{2}$$

Here g is the acceleration of gravity (9.54 m/s^2), N is the buoyancy frequency (estimated at 0.018 s^{-1} using the lidar profiles), λ_z is the vertical wavelength (measured directly from the lidar data, e.g., Figure 9), and λ_x is the horizontal wavelength (estimated by the average value between two central saw-tooth bands as measured by the AMTM, e.g., Figure 6). This equation is an approximation for long horizontal wavelengths, implying a bias of ~10% for λ_x ~ 50 km and λ_z ~ 15 km (Ern et al., 2017). Nonlinear behavior such as the one exhibited by the 21 June MW may also affect the results (Ern et al., 2004). This said, this equation still provides a good estimate of the wave MF and its variability during the event.

Calculated using equation (2) and the measured MW parameters (e.g., Table 1**)**, the estimated momentum fluxes (MF) during the course of this MW event exhibit three large well-defined peaks in MF amplitudes ranging from 400 to 800 m^2/s^2, as shown in Figure 12, which plots the MF versus UT time (3-point averaged). The uncertainty Δ(MF) on the MF calculation is given by the equation

$$\Delta\mathrm{MF} = \sqrt{\left(\frac{\mathrm{MF}}{\lambda_z}\right)^2(\Delta\lambda_z)^2 + \left(\frac{\mathrm{MF}}{\lambda_x}\right)^2(\Delta\lambda_x)^2 + 2\left(\frac{\mathrm{MF}}{N}\right)^2(\Delta N)^2 + 2\left(\frac{\mathrm{MF}}{\frac{T'}{T_0}}\right)^2\Delta\left(\frac{T'}{T_0}\right)^2} \tag{3}$$

where Δ represents the uncertainty on each variable, with $\Delta\lambda_x = \Delta\lambda_z = 5$ km, $\Delta N = 0.002$ s^{-1}, and $\Delta(T'/T_0)$ as determined by equation (1).

Within the limits of our measurements, Figure 12 clearly establishes a high level of sustained MFs and implied MLT forcing (>400 m^2/s^2) for most of the event (>1.5 hr). The oscillation observed in Figure 11 appears as three distinct peaks with magnitudes ranging from ~600 to 800 m^2/s^2, driven strongly by the large T'/T_0 perturbations. While variations in the average λ_x (~50–65 km) and the reduction in λ_z (~40%) were

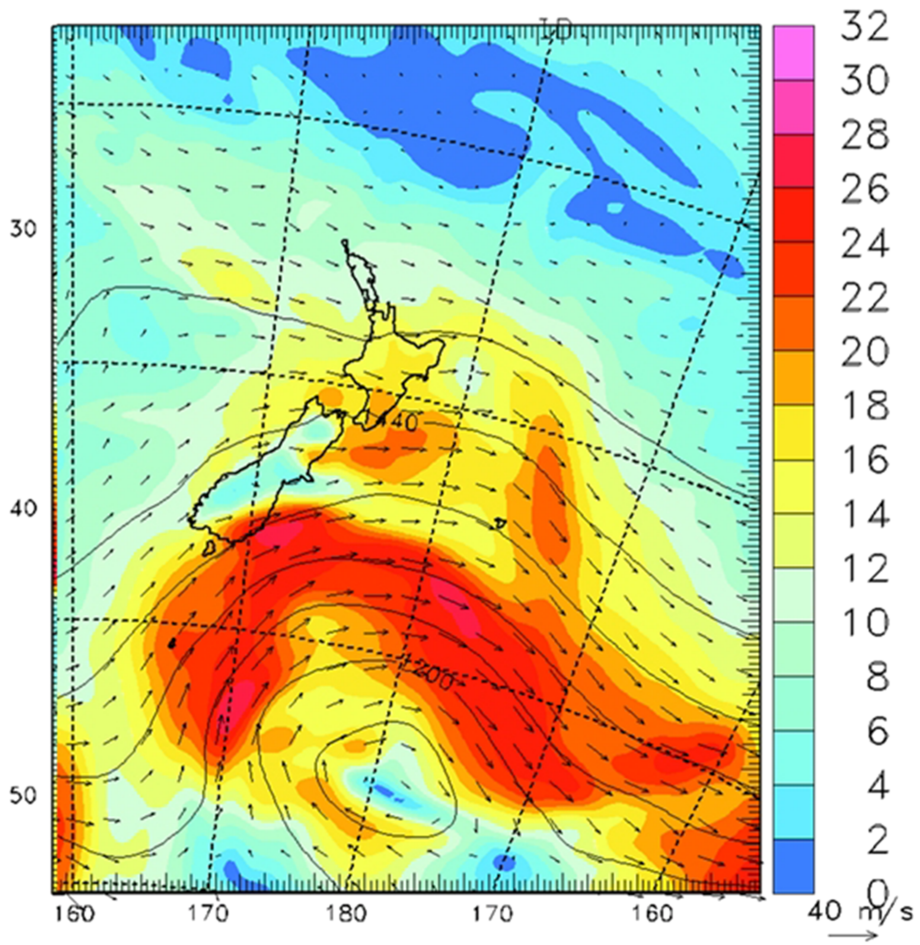

Figure 13. U.S. Navy Coupled Ocean-Atmosphere Mesoscale Prediction System map showing the horizontal wind at 850 hPa (1,500-m altitude) over New Zealand and its surrounding oceans, at 06 UT on 21 June 2014. The prevailing near-surface winds were northeastward and small (<10 m/s). This analysis suggests that weak wind forcing over the ~N-S aligned lower altitude mountain ridges on the southern end of the South Island (Figure 7b) was the most likely source of this exceptional mesospheric event.

significant during this event, they were not found to affect the overall periodic variation in MF seen in Figure 12. The observed variations in MF are therefore directly related to changes in the MW amplitude in the MLT region. Such amplitudes and MF variations at high altitudes can have several causes. Variable forcing at lower altitudes in space and time can modulate MW forcing, influencing amplitudes, and dominant scales at higher altitudes. Varying winds through which the MWs propagate can modulate MW phase speeds and vertical group velocities on short time scales. Additionally, MW instability dynamics in the mesosphere impose significant MF modulation at a given altitude due to the effects of MW breaking at this altitude and below. GW breaking, in general, yields significant reductions in the GW amplitude and larger fractional MF reductions (Fritts et al., 2009b), but it does not eliminate the GW. Hence, successive propagation to higher altitudes will restore the GW amplitude on a timescale dictated approximately by propagation over a vertical wavelength, or that fraction that exhibited strong dissipation. This time is the GW intrinsic period, $T_{GW} \sim T_b\lambda_x/\lambda_z \sim$ 25–30 min, for $T_b = 2\pi/N \sim$ 5.8 min and the approximately hydrostatic MWs having $\lambda_x \sim$ 40–60 km and $\lambda_z \sim$ 10–12 km. Given these expected dynamics and the observed MF modulation timescale, MW breaking dynamics seem most likely to have accounted for the observed variability in MW MFs over this interval. Indeed, as discussed in *F19*, the occurrences of strong instability dynamics associated with this breaking MW event appear to correlate well with the minima in the MW MFs show in Figure 12.

4.2. Tropospheric MW Source Region

For the DEEPWAVE mission our expectation for MW generation was for strong southeastward tropospheric winds impinging upon the towering NE-SW aligned Southern Alps (see Figure 1). The mission was conducted during Austral Winter when such prevailing winds are expected to be strong. Figure 13 shows the U.S. Naval Research Laboratory Coupled Ocean–Atmosphere Mesoscale Prediction System map (Doyle et al., 2011; Hodur, 1997) for the prevailing winds at 850 hPa (~1,500-m altitude) over NZ and its surrounding oceans, at 06 UT on 21 June 2014. During this night, the synoptic conditions, as shown in Figure 13, were characterized by northeastward near-surface winds (<10 m/s) blowing over the southern SI, essentially parallel to the backbone of the Southern Alps. This situation is quite different from that expected for significant MW generation (e.g., by southeastward flow). However, close inspection of the contour map of Figure 1 also identifies several extended ~N-S aligned mountain ridges (>1,000 m) and valleys in the southern part of the SI, extending away from the broad backbone of the Southern Alps. Figure 13 shows that the prevailing northeastward winds impinged upon these ridges, preferentially creating the observed N-S aligned MW. Indeed, the sketch in Figure 7b shows that the mesospheric MW structures occurred over this region and exhibited remarkably good alignment with the local mountain ridges suggesting they were the most likely the orographic source of this MW event.

5. Summary

These joint DEEPWAVE measurements have enabled an in-depth investigation of this remarkable MW event observed on 21 June 2014 over the New Zealand South Island. In particular, we have been able to investigate its unusual saw-tooth spatial structure, temporal evolution, and its most likely source, as well as quantify the horizontal and vertical wavelengths, geographic extent, and perturbation amplitudes leading to confident estimates of the MW structure, variability, and MFs.

Key results are as follows:

1. Novel mesospheric MW characteristics dominated by an unusual saw-tooth structure that was most prominent in the OH temperature maps exhibiting broad warm phases separated by narrow cold phases (typically 5- to 8-km wide) and dominant horizontal wavelengths ranging from ~40 to 70 km (Table 1). To our best knowledge, this is the first evidence documenting the development of such structures and their implications for MW breaking in the MLT region (also see F19).
2. The estimated MFs for this event were among the largest ever reported, as large as ~600–800 m^2/s^2, and exhibited three distinct peaks spaced by ~25 min. Several causes of the variable MFs seemed possible, but the temporal variability of MW breaking appeared to us to be the most likely explanation.
3. Unexpected wind forcing over the lower N-S aligned mountain ridges on the southern end of the SI, rather than over the spine of the Southern Alps, was determined to be the most likely source of this exceptional mesospheric event.
4. Combined wind data reveal a consistent, strong eastward flow enabling the MWs to propagate from their identified orographic source region up through the middle atmosphere (without significant attenuation, see F19) into the MLT region. Furthermore, the MWs were most prominent and coherent in the OH emission (altitude ~82 km) during a sustained ~2-hr period of strong >60 m/s eastward winds favorable to MW propagation.
5. Joint ground-based measurements indicated that this MW event extended over a much larger geographic area encompassing the SI and the surrounding oceans (>200,000 km^2) helping establish the regional hot spot influence on the MLT region.
6. A Rayleigh lidar revealed coherent MW propagation from the middle stratosphere into the MLT. Concurrent O_2 and OI (557.7 nm) all-sky image data from Lauder (not shown) further identified similar MW structure, indicating that this event extended to higher altitudes (at least 10 km above the OH layer).

During the DEEPWAVE campaign coordinated ground-based measurements were made nightly over a 6-week period resulting in the detection of mesospheric MW signatures on 28 nights out of a total of 40 clear or partially clear nights. These novel MW observations suggest a high frequency of occurrence (~70%) for MW able to regularly penetrate into the MLT region and establishing orographic forcing as a significant source of mesospheric wave activity during the winter season.

In summary, the remarkable event on 21 June 2014 was one of the largest and sustained MW breaking events yet measured. As far as we are aware, this is the first identification of MW MF temporal variability and its likely causes. These new results strongly suggest that MWs at small horizontal scales (<100 km) can play large (and highly variable) roles in the local/regional momentum budget in the MLT region when forcing and propagation conditions allow them to reach mesospheric altitudes with large amplitudes.

Acknowledgments
The collaborative research described herein was supported by several NSF grants gratefully cited in GEMS. The authors wish to especially acknowledge the National Institute of Water and Atmospheric Research of New Zealand (NIWA) for hosting the AMTM, Lidar, and all-sky imager operations during the DEEPWAVE mission. In particular, we wish to thank D. Holland and J. Robinson for their considerable help with setting up and maintaining the instruments at Lauder. We also deeply thank the NCAR/EOL personnel for their tremendous contribution to the DEEPWAVE program. Likewise, we thank the Mount John Observatory for supporting the operations of the FPI. B. K. thanks the German Research Foundation (DFG) for support through the research unit "MSG-GWaves project RA1400/6-1". S.D.E. acknowledges support of the Chief of Naval Research for the NAVGEM reanalyzes reported here. USU further acknowledges R. Esplin and D. McLain, at the Space Dynamics Laboratory, for their expertise and help in the development of the AMTM. We also acknowledge the NASA TIMED program for the SABER data used in these analyses. Finally, we gratefully acknowledge the U.S. Antarctic Program for hosting the DEEPWAVE field campaign operations from their facilities in Christchurch, New Zealand. The DEEPWAVE data used in these analyses are available on the NCAR EOL archive at www.eol.ucar.edu/field_projects/deepwave. The link to the HALO database that hosts the lidar data used in the paper is https://halo-db.pa.op.dlr.de/mission/24.

References

Alexander, M. J., & Grimsdell, A. W. (2013). Seasonal cycle of orographic gravity wave occurrence above small islands in the Southern Hemisphere: Implications for effects on the general circulation. *Journal of Geophysical Research: Atmospheres*, *118*, 11,589–11,599. https://doi.org/10.1002/2013JD020526

Alexander, M. J., & Teitelbaum, H. (2007). Observation and analysis of a large amplitude mountain wave event over the Antarctic Peninsula. *Journal of Geophysical Research*, *112*, D21103. https://doi.org/10.1029/2006JD008368

Baker, D. J., & Stair, A. T. (1988). Rocket measurements of the altitude distribution of the hydroxyl airglow. *Physica Scripta*, *37*(4), 611–622. https://doi.org/10.1088/0031-8949/37/4/021

Baumgardner, J., Wroten, J., Semeter, J., Kozyra, J., Buonsato, M., Erickson, P., & Mendillo, M. (2007). A very bright SAR arc: Implications for extreme magnetosphere-ionosphere coupling. *Annales Geophysicae*, *25*, 2593–2608. https://doi.org/10.5194/angeo-25-2593-2007

Bossert, K., Fritts, D. C., Heale, C. J., Eckermann, S. D., Plane, J. M. C., Snively, J. B., et al. (2018). Momentum flux spectra of a mountain wave event over New Zealand. *Journal of Geophysical Research: Atmospheres*, *123*, 9980–9991. https://doi.org/10.1029/2018JD028319

Bossert, K., Fritts, D. C., Pautet, P.-D., Williams, B. P., Taylor, M. J., Kaifler, B., et al. (2015). Momentum flux estimates accompanying multiscale gravity waves over Mount Cook, New Zealand, on 13 July 2014 during the DEEPWAVE campaign. *Journal of Geophysical Research: Atmospheres*, *120*, 9323–9337. https://doi.org/10.1002/2015JD023197

Bossert, K., Kruse, C. G., Heale, C. J., Fritts, D. C., Williams, B. P., Snively, J. B., et al. (2017). Secondary gravity wave generation over New Zealand during the DEEPWAVE campaign. *Journal of Geophysical Research: Atmospheres*, *122*, 7834–7850. https://doi.org/10.1002/2016JD02607

Bougeault, P., Binder, P., Buzzi, A., Dirks, R., Kuettner, J., Houze, R., et al. (2001). The MAP special observing period. *Bulletin of the American Meteorological Society*, *82*(3), 433–462. https://doi.org/10.1175/1520-0477

Broutman, D., Eckermann, S. D., Knight, H., & Ma, J. (2017). A stationary phase solution for mountain waves with application to mesospheric mountain waves generated by Auckland Island. *Journal of Geophysical Research: Atmospheres*, *122*, 699–711. https://doi.org/10.1002/2016JD025699

Conner, J. F., Smith, R. W., & Hernandez, G. (1993). Techniques for deriving Doppler temperatures from multiple-line Fabry–Perot profiles: an analysis. *Applied Optics*, *32*(23), 4437–4444. https://doi.org/10.1364/AO.32.004437

Doyle, J. D., Jiang, Q., Smith, R. B., & VGrubišić, V. (2011). Three-dimensional characteristics of stratospheric mountain waves during T-REX. *Monthly Weather Review*, *139*, 3–23. https://doi.org/10.1175/2010MWR3466.1

Dunkerton, T. J. (1997). The role of gravity waves in the quasi-biennial oscillation. *Journal of Geophysical Research*, *102*(D22), 26,053–26,076 . https://doi.org/10.1029/96JD02999

Dunkerton, T. J., & Butchart, N. (1984). Propagation and selective transmission of internal gravity waves in a sudden warming. *Journal of the Atmospheric Sciences*, *41*(8), 1443–1460. https://doi.org/10.1175/1520-0469(1984)041<1443:PASTOI>2.0.CO;2

Durran, D. R. (1990). Mountain waves and downslope winds. In *Atmospheric processes over complex terrain Meteorological Monographs* (Vol. 23, pp. 59–81). Boston, MA: American Meteorological Society. https://doi.org/10.1007/978-1-935704-25-6_4

Eckermann, S. D., Broutman, D., Ma, J., Doyle, J. D., Pautet, P.-D., Taylor, M. J., et al. (2016). Dynamics of orographic gravity waves observed in the mesosphere over the Auckland Islands during the Deep Propagating Gravity Wave Experiment (DEEPWAVE). *Journal of the Atmospheric Sciences*, *73*, 3855–3876. https://doi.org/10.1175/JAS-D-16-0059.1

Ehard, B., Kaifler, B., Kaifler, N., & Rapp, M. (2015). Evaluation of methods for gravity wave extraction from middle-atmospheric lidar temperature measurements. *Atmospheric Measurement Techniques*, *8*, 4645–4655. https://doi.org/10.5194/amt-8-4645-2015

Ern, M., Hoffmann, L., & Preusse, P. (2017). Directional gravity wave momentum fluxes in the stratosphere derived from high-resolution AIRS temperature data. *Geophysical Research Letters*, *44*, 475–485. https://doi.org/10.1002/2016GL072007

Ern, M., Preusse, P., Alexander, M. J., & Warner, C. D. (2004). Absolute values of gravity wave momentum flux derived from satellite data. *Journal of Geophysical Research*, *109*, D20103. https://doi.org/10.1029/2004JD004752

Ern, M., Trinh, Q. T., Preusse, P., Gille, J. C., Mlynczak, M. G., Russell, J. M. III, & Riese, M. (2018). GRACILE: A comprehensive climatology of atmospheric gravity wave parameters based on satellite limb soundings. *Earth System Science Data*, *10*, 857–892. https://doi.org/10.5194/essd-10-857-2018

Fritts, D. C., & Alexander, M. J. (2003). Gravity dynamics and effects in the middle atmosphere. *Reviews of Geophysics*, *41*(1), 1003. https://doi.org/10.1029/2001RG000106

Fritts, D. C., Pautet, P.-D., Bossert, K., Taylor, M. J., Williams, B. P., Iimura, H., et al. (2014). Quantifying gravity wave momentum fluxes with Mesosphere Temperature Mappers and correlative instrumentation. *Journal of Geophysical Research: Atmospheres*, *119*, 13,583–13,603. https://doi.org/10.1002/2014JD022150

Fritts, D. C., & Rastogi, P. K. (1985). Convective and dynamical instabilities due to gravity wave motions in the lower and middle atmosphere: Theory and observations. *Radio Science*, *20*(6), 1247–1277. https://doi.org/10.1029/RS020i006p01247

Fritts, D. C., Smith, R. B., Taylor, M. J., Doyle, J. D., Eckermann, S. D., Dörnbrack, A., et al. (2016). The Deep Propagating Gravity Wave Experiment (DEEPWAVE): An airborne and ground-based exploration of gravity wave propagation and effects from their sources throughout the lower and middle atmosphere. *Bulletin of the American Meteorological Society*, *97*, 425–453. https://doi.org/10.1175/BAMS-D-14-00269.1

Fritts, D. C., Taylor, M. J., Pautet, P.-D., Criddle, N. R., Kaifler, B., Wang, L., et al. (2019). Large-amplitude mountain waves in the mesosphere observed on 21 June 2014 during DEEPWAVE: 2. Nonlinear dynamics, wave breaking, and instabilities. *Journal of Geophysical Research: Atmospheres*, *124*. https://doi.org/10.1029/2019JD030899

Fritts, D. C., Vadas, S. A., & Yamada, Y. (2002). An estimate of strong local gravity wave body forcing based on OH airglow and meteor radar observations. *Geophysical Research Letters*, *29*(10), 1429. https://doi.org/10.1029/2001GL013753

Fritts, D. C., & Vincent, R. A. (1987). Mesospheric momentum flux studies at Adelaide, Australia: Observations and a gravity wave/tidal interaction model. *Journal of the Atmospheric Sciences*, *44*(3), 605–619. https://doi.org/10.1175/1520-0469(1987)044<0605:MMFSAA>2.0.CO;2

Fritts, D. C., Vosper, S. B., Williams, B. P., Bossert, K., Plane, J. M. C., Taylor, M. J., et al. (2018). Large-amplitude mountain waves in the mesosphere accompanying weak cross mountain flow during DEEPWAVE Research Flight RF22. *Journal of Geophysical Research: Atmospheres*, *123*, 9992–10,022. https://doi.org/10.1029/2017JD028250

Fritts, D. C., Wang, L., Geller, M. A., Lawrence, D. A., Werne, J., & Balsley, B. B. (2016). Numerical modeling of multi-scale dynamics at a high Reynolds number: Instabilities, turbulence, and an assessment of Ozmidov and Thorpe scales. *Journal of the Atmospheric Sciences*, *73*, 555–578. https://doi.org/10.1175/JAS-D-14-0343.1

Fritts, D. C., Wang, L., Werne, J., Lund, T., & Wan, K. (2009a). Gravity wave instability dynamics at high Reynolds numbers, 2: Turbulence evolution, structure, and anisotropy. *Journal of the Atmospheric Sciences*, *66*, 1149–1171. https://doi.org/10.1175/2008JAS2727.1

Fritts, D. C., Wang, L., Werne, J., Lund, T., & Wan, K. (2009b). Gravity wave instability dynamics at high Reynolds numbers, 1: Wave field evolution at large amplitudes and high frequencies. *Journal of the Atmospheric Sciences*, *66*, 1126–1148. https://doi.org/10.1175/2008JAS2726.1

Fritts, D. C., Wang, L., & Werne, J. A. (2013). Gravity wave-fine structure interactions. Part I: Influences of fine structure form and orientation on flow evolution and instability. *Journal of the Atmospheric Sciences*, *70*, 3710–3734. https://doi.org/10.1175/JAS-D-13-055.1

Garcia, R. R., & Solomon, S. (1985). The effect of breaking gravity waves on the dynamical and chemical composition of the mesosphere and lower thermosphere. *Journal of Geophysical Research*, *90*(D2), 3850–3868. https://doi.org/10.1029/JD090iD02p03850

Heale, C. J., Bossert, K., Snively, J. B., Fritts, D. C., Pautet, P.-D., & Taylor, M. J. (2017). Numerical modeling of a multiscale gravity wave event and its airglow signatures over Mount Cook, New Zealand during the DEEPWAVE campaign. *Journal of Geophysical Research: Atmospheres*, *122*, 846–860. https://doi.org/10.1002/2016JD025700

Hendricks, E. A., Doyle, J. D., Eckermann, S. D., Jiang, Q., & Reinecke, P. A. (2014). What is the source of the stratospheric gravity wave belt in Austral winter? *Journal of the Atmospheric Sciences*, *71*, 1583–1592. https://doi.org/10.1175/JAS-D-13-0332.1

Hernandez, G., & McCarthy, M. P. (2011). Long-term instrumental parameter investigation of a Fabry–Perot spectrometer at an isolated field station. *Applied Optics*, *50*, 1951–1957. https://doi.org/10.1364/AO.50.001951

Hernandez, G., & Mills, O. A. (1973). Feedback stabilized Fabry-Perot interferometer. *Applied Optics*, *12*(1), 126–130. https://doi.org/10.1364/AO.12.000126

Hernandez, G., & Smith, R. W. (1995). Winds and vertical wavelengths deduced from the ground-based measurement of the Doppler shifts of the $O_2(b\ ^1\sum_g + - X\ ^3\sum_g -)$, $OI(^1D_2 - ^1S_0)$, and the $X^2\Pi$ OH (6-2) Band $P_1(2)$ line emissions in the mid-latitude upper middle atmosphere. *Geophysical Research Letters*, *22*(4), 369–372. https://doi.org/10.1029/94GL03114

Hocke, K., & Tsuda, T. (2001). Gravity waves and ionospheric irregularities over tropical convection zones observed by GPS/MET radio occultation. *Geophysical Research Letters*, *28*(14), 2815–2818. https://doi.org/10.1029/2001GL013076

Hodur, R. M. (1997). The Naval Research Laboratory's Coupled Ocean/Atmospheric Mesoscale Prediction System (COAMPS). *Monthly Weather Review*, *125*(7), 1414–1430. https://doi.org/10.1175/1520-0493(1997)125<1414:TNRLSC>2.0.CO;2

Hoffmann, L., Xue, X., & Alexander, M. J. (2013). A global view of stratospheric gravity wave hotspots located with Atmospheric Infrared Sounder observations. *Journal of Geophysical Research: Atmospheres*, *118*, 416–434. https://doi.org/10.1029/2012JD018658

Hogan, T. F., Liu, M., Ridout, J. S., Peng, M. S., Whitcomb, T. R., Ruston, B. C., et al. (2014). The Navy Global Environmental Model. *Oceanography*, *27*, 116–125. https://doi.org/10.5670/oceanog.2014.73

Holton, J. R. (1982). The role of gravity wave induced drag and diffusion in the momentum budget of the mesosphere. *Journal of the Atmospheric Sciences*, *39*(4), 791–799. https://doi.org/10.1175/1520-0469(1982)039<0791:TROGWI>2.0.CO;2

Holton, J. R. (1984). The generation of mesospheric planetary waves by zonally asymmetric gravity wave breaking. *Journal of the Atmospheric Sciences*, *41*(23), 3427–3430. https://doi.org/10.1175/1520-0469(1984)041<3427:TGOMPW>2.0.CO;2

Hoppel, K. W., Eckermann, S. D., Coy, L., Nedoluha, G. E., Allen, D. R., Swadley, S. D., & Baker, N. L. (2013). Evaluation of SSMIS upper atmosphere sounding channels for high-altitude data assimilation. *Monthly Weather Review*, *141*, 3314–3330. https://doi.org/10.1175/MWR-D-13-00003.1

Jiang, J. H., Eckermann, S. D., Wu, D. L., & Ma, J. (2004). A search for mountain waves in MLS stratospheric limb radiances from the winter Northern Hemisphere: Data analysis and global Mountain wave modeling. *Journal of Geophysical Research*, *109*, D03107. https://doi.org/10.1029/2003JD003974

Jiang, J. H., Wang, K., Goya, K., Hocke, K., Eckermann, S. D., Ma, J., et al. (2004). Geographical distribution and interseasonal variability of tropical deep convection: UARS MLS observations and analyses. *Journal of Geophysical Research*, *109*, D03111. https://doi.org/10.1029/2003JD003756

Jiang, J. H., Wu, D. L., Eckermann, S. D., & Ma, J. (2003). Mountain waves in the middle atmosphere: Microwave limb sounder observations and analyses. *Advances in Space Research*, *32*(5), 801–806. https://doi.org/10.1016/S0273-1177(03)00402-2

Kaifler, B., Kaifler, N., Ehard, B., Dörnbrack, A., Rapp, M., & Fritts, D. C. (2015). Influences of source conditions on mountain wave penetration into the stratosphere and mesosphere. *Geophysical Research Letters*, *42*, 9488–9494. https://doi.org/10.1002/2015GL066465

Klemp, J. B., & Lilly, D. K. (1978). Numerical simulation of hydrostatic mountain waves. *Journal of the Atmospheric Sciences*, *35*(1), 78–107. https://doi.org/10.1175/1520-0469(1978)035<0078:NSOHMW>2.0.CO;2

Liley, J. B., & Forgan, B. W. (2009). Aerosol optical depth over Lauder, New Zealand. *Geophysical Research Letters*, *36*, L07811. https://doi.org/10.1029/2008GL037141

Lilly, D. K., & Kennedy, P. J. (1973). Observations of a stationary mountain wave and its associated momentum flux and energy dissipation. *Journal of the Atmospheric Sciences*, *30*(6), 1135–1152. https://doi.org/10.1175/1520-0469(1973)030<1135:OOASMW>2.0.CO;2

Lindzen, R. S. (1981). Turbulence and stress owing to gravity wave and tidal breakdown. *Journal of Geophysical Research*, *86*(C10), 9707–9714. https://doi.org/10.1029/JC086iC10p09707

Lombard, P. N., & Riley, J. J. (1996). On the breakdown into turbulence of propagating internal waves. *Dynamics of Atmospheres and Oceans*, *23*(1-4), 345–355. https://doi.org/10.1016/0377-0265(95)00431-9

McFarlane, N. A. (1987). The effect of orographically excited gravity wave drag on the general circulation of the lower stratosphere and troposphere. *Journal of the Atmospheric Sciences*, *44*(14), 1775–1800. https://doi.org/10.1175/1520-0469(1987)044<1775:TEOOEG>2.0.CO;2

McLandress, C., Shepherd, T. G., Polavarapu, S., & Beagley, S. (2012). Is missing orographic gravity wave drag near 60S the cause of the stratospheric zonal wind biases in chemistry-climate models? *Journal of the Atmospheric Sciences*, *69*, 802–818. https://doi.org/10.1175/JAS-D-11-0159.1

McLaughlin, P. F. (2018). The Advanced Mesospheric Temperature Mapper: Remote sensing of the nighttime OH layer during the DEEPWAVE and Super Soaker campaigns. MS.c, Department of Physics, Utah State University.

Meriwether, J. W. Jr. (1975). High latitude airglow observations of correlated short-term fluctuations in the hydroxyl Meinel 8–3 band intensity and rotational temperature. *Planetary and Space Science*, *23*(8), 1211–1221. https://doi.org/10.1016/0032-0633(75)90170-1

Mulligan, F. J., Dyrland, M. E., Sigernes, F., & Deehr, C. S. (2009). Inferring hydroxyl layer peak heights from ground-based measurements of OH(6-2) band integrated emission rate at Longyearbyen (78°N, 16°E). *Annales Geophysicae*, *27*, 4197–4205. https://doi.org/10.5194/angeo-27-4197-2009

Nakamura, T., Tsuda, T., Yamamoto, M., Fukao, S., & Kato, S. (1993). Characteristics of gravity waves in the mesosphere observed with the middle and upper atmosphere radar 1. Momentum flux. *Journal of Geophysical Research*, *98*(D5), 8899–8910. https://doi.org/10.1029/92JD02978

Ortland, D. A., & Alexander, M. J. (2006). Gravity wave influence on the global structure of the diurnal tide in the mesosphere and lower thermosphere. *Journal of Geophysical Research*, *111*, A10S10. https://doi.org/10.1029/2005JA011467

Palmer, T. N., Shutts, G. J., & Swinbank, R. (1986). Alleviation of a systematic westerly bias in general circulation and numerical weather prediction models through an orographic gravity wave drag parameterization. *Quarterly Journal of the Royal Meteorological Society*, *112*(474), 1001–1039. https://doi.org/10.1002/qj.49711247406

Pautet, P.-D., Taylor, M. J., Fritts, D. C., Bossert, K., Williams, B. P., Broutman, D., et al. (2016). Large-amplitude mesospheric response to an orographic wave generated over the Southern Ocean Auckland Islands (50.7°S) during the DEEPWAVE project. *Journal of Geophysical Research: Atmospheres*, *121*, 1431–1441. https://doi.org/10.1002/2015JD024336

Pautet, P.-D., Taylor, M. J., Pendleton, W. R. Jr., Zhao, Y., Yuan, T., Esplin, R., & McLain, D. (2014). Advanced Mesospheric Temperature Mapper for high-latitude airglow studies. *Applied Optics*, *53*, 5934–5943. https://doi.org/10.1364/AO.53.005934

Pautet, P.-D., Taylor, M. J., Snively, J. B., & Solorio, C. (2018). Unexpected occurrence of mesospheric frontal gravity wave events over South Pole (90°S). *Journal of Geophysical Research: Atmospheres*, *123*, 160–173. https://doi.org/10.1002/2017JD027046

Reid, I. M., & Vincent, R. A. (1987). Measurements of mesospheric gravity wave momentum fluxes and mean flow accelerations at Adelaide, Australia. *Journal of Atmospheric and Solar-Terrestrial Physics*, *49*(5), 443–460. https://doi.org/10.1016/0021-9169(87)90039-0

Smith, A. K. (2003). The origin of stationary planetary waves in the upper mesosphere. *Journal of the Atmospheric Sciences*, *60*(24), 3033–3041. https://doi.org/10.1175/1520-0469(2003)060<3033:TOOSPW>2.0.CO;2

Smith, R. B., Woods, B. K., Jensen, J., Cooper, W. A., Doyle, J. D., Jiang, Q., & Grubisic, V. (2008). Mountain waves entering the stratosphere. *Journal of the Atmospheric Sciences*, *65*, 2543–2562. https://doi.org/10.1175/2007JAS2598.1

Smith, S., Baumgardner, J., & Mendillo, M. (2009). Evidence of mesospheric gravity-waves generated by orographic forcing in the troposphere. *Geophysical Research Letters*, *36*, L08807. https://doi.org/10.1029/2008GL036936

Sonmor, L. J., & Klaassen, G. P. (1997). Toward a unified theory of gravity wave stability. *Journal of the Atmospheric Sciences*, *54*(22), 2655–2680. https://doi.org/10.1175/1520-0469

Stephan, C. C., Strube, C., Klocke, D., Ern, M., Hoffmann, L., Preusse, P., & Schmidt, H. (2019). Gravity waves in global high-resolution simulations with explicit and parameterized convection. *Journal of Geophysical Research: Atmospheres*, *124*, 4446–4459. https://doi.org/10.1029/2018JD030073

Taylor, M. J., Pautet, P.-D., Medeiros, A. F., Buriti, R., Fechine, J., Fritts, D. C., et al. (2009). Characteristics of mesospheric gravity waves near the magnetic equator, Brazil, during the SpreadFEx campaign. *Annales Geophysicae*, *27*, 461–472. https://doi.org/10.5194/angeo-27-461-2009

Taylor, M. J., Pendleton, W. R. Jr., Clark, S., Takahashi, H., Gobbi, D., & Goldberg, R. A. (1997). Image measurements of short-period gravity waves at equatorial latitudes. *Journal of Geophysical Research*, *102*(D22), 26,283–26,299. https://doi.org/10.1029/96JD03515

Vadas, S. L., & Fritts, D. C. (2002). The importance of spatial variability in the generation of secondary gravity waves from local body forces. *Geophysical Research Letters*, *29*(20), 1984. https://doi.org/10.1029/2002GL015574

Vadas, S. L., & Liu, H.-L. (2009). The generation of large-scale gravity waves and neutral winds in the thermosphere from the dissipation of convectively-generated gravity waves. *Journal of Geophysical Research*, *114*, A10310. https://doi.org/10.1029/2009JA014108

Vincent, R. A., & Reid, I. M. (1983). HF Doppler measurements of mesospheric momentum fluxes. *Journal of the Atmospheric Sciences*, *40*(5), 1321–1333. https://doi.org/10.1175/1520-0469(1983)040<1321:HDMOMG>2.0.CO;2

von Savigny, C., McDade, I. C., Eichmann, K.-U., & Burrows, J. P. (2012). On the dependence of the OH* Meinel emission altitude on vibrational level: SCIAMACHY observations and model simulations. *Atmospheric Chemistry and Physics Discussions*, *12*, 5817–5849. https://doi.org/10.5194/acpd-12-5817-2012

Yamada, Y., Fukunishi, H., Nakamura, T., & Tsuda, T. (2001). Breakdown of small-scale quasi-stationary gravity wave and transition to turbulence observed in OH airglow. *Geophysical Research Letters*, *28*(11), 2153–2156. https://doi.org/10.1029/2000GL011945

Yuan, T., Pautet, P.-D., Zhao, Y., Cai, X., & Taylor, M. J. (2014). Coordinated investigation of mid-latitude upper mesospheric temperature inversion layers and the associated gravity wave forcing by Na lidar and Advanced Mesospheric Temperature Mapper at Logan, Utah (42°N). *Journal of Geophysical Research: Atmospheres*, *119*, 3756–3769. https://doi.org/10.1002/2013jd020586

Zhao, Y., Taylor, M. J., & Chu, X. (2005). Comparison of simultaneous Na lidar and Mesospheric Temperature Mapper measurements and the effects of tides on the emission layer heights. *Journal of Geophysical Research*, *110*, D09S07. https://doi.org/10.1029/2004JD005115